FINITE ELEMENT ANALYSES OF A CYCLICALLY LOADED LINEAR VISCOELASTIC BIODEGRADABLE STENT

A Thesis

by

JASON KYLE MURPHY

Submitted to the Office of Graduate and Professional Studies of
Texas A&M University
in partial fulfillment of the requirements for the degree of

MASTER OF SCIENCE

Chair of Committee,	Anastasia Muliana
Committee Members,	Amine Benzerga
	Sevan Goenezen
Head of Department,	Andreas A. Polycarpou

December 2014

Major Subject: Mechanical Engineering

ABSTRACT

Biodegradable polymers have been in use for biomedical applications such as sutures and various implants for many years. In the recent decade, research into the development of biodegradable cardiac stents has expanded. This is due to a need for a stent to perform its job and then be removed from the site of implantation, as up to 20% of all cases require re-intervention after 6 – 12 months due to in-stent restenosis, as reported in 2010.

In this study, the effect of viscoelastic and mechanical degradation behaviors on the performance of cylindrical annuli that mimic stents under cyclic loadings is examined. Two polymers are considered: poly-L-lactic acid (PLLA) and polyoxymethylene (POM). A numerical algorithm for an isotropic, linear, viscoelastic material with inclusion of degradation is developed and incorporated into the finite element software ABAQUS/CAE via a user-defined material subroutine (UMAT). A constant pressure meant to mimic the arterial wall's resistance to expansion is coupled with a cyclic pressure equivalent to an ideal resting blood pressure. The degradation considered is defined as strain-induced. Loading is applied under two cases. A linearly ramped loading is first studied, followed by a creep-cyclic study.

Circumferential stresses and strains, along with the degradation, are presented for both a simplified cylindrical annulus, as well as two typical real-world stent geometries. It is seen that not only do material properties affect deformation, but geometrical properties have a large effect as well. The uniform stresses and strains developed in the

cylindrical annulus are far less than the non-uniform stresses and strains observed in the realistic stent geometries. This is due to localized stress and strains at the junctions in the mesh of the realistic geometries, where stress concentrations are a maximum. As predicted by the time-dependent material properties given for each material from previous experimental studies, the stresses, strains, and degradation observed are strongly dependent on the time-dependent material behaviors.

ACKNOWLEDGEMENTS

I would like to thank my adviser, Dr. Anastasia Muliana, for giving me an opportunity to reach my goals, as well as for her guidance and patience as I worked through my Master's degree. For all of my professors, classmates, and colleagues that have helped me along the way, I extend my gratitude.

I would like to thank Texas A&M's Department of Mechanical Engineering and Texas A&M's Supercomputing Facility for granting me access to the necessary tools needed to complete my research.

I would also like to thank my family and friends for their support at times when I needed it most. Without their encouragement, I would not have accomplished the things that I have in life.

Most of all, I thank my wife, Christie, for the seven wonderful years.

TABLE OF CONTENTS

LIST OF FIGURES

LIST OF TABLES

CHAPTER I

INTRODUCTION AND LITERATURE REVIEW

1.1 Cardiovascular Disease

Over the past century, cardiovascular diseases (CVD) have remained at the top of the list as the primary causes of death of Americans. As of today, the Center for Disease Control and Prevention estimates that CVD account for over one-third (33.6%) of all US deaths [6]. According to the American Heart Association, total costs associated with CVD amounted to $368.4 billion USD in 2004, with an increase to $403.1 billion USD as of 2006 [2, 9]. In 2010, the trend continued as the total cost of CVD showed an increase, as the estimated cost in the US was approximately $444 billion USD [6]. This amounted to the treatment of these diseases costing approximately one dollar of every six dollars spent on health care in the country [6].

Of the forms of cardiovascular disease, atherosclerosis is one of the most critical. Rather than being distributed uniformly throughout the cardiovascular system, atherosclerosis is a progressive CVD that develops in the arteries around the heart and the arteries leading to the brain and legs, known as the coronary, carotid and femoral, respectively [2, 3]. Defined as the hardening of the arteries, atherosclerosis occurs when plaque builds up and attaches to the lumen inside the vessels. As this occurs, blood flow is restricted resulting in the loss of the supply of oxygen and glucose to the distal tissues which are needed for cellular metabolism, a condition known as ischemia. As a result, the individual cells in the tissues cannot survive and the tissues become compromised

and vulnerable. To prevent this sort of damage, cardiovascular intervention is needed in order to restore blood flow to maintain a healthy cardiovascular system.

1.2 Early Cardiovascular Intervention

Early cardiovascular interventions were open surgeries such as coronary artery bypass graft surgery (CABG). Introduced in the 1960s, CABG is performed by connecting a healthy artery or vein from elsewhere in the body to the stenotic vessel in a manner that bypasses the blocked section. As a result, this provides a new obstruction free path for blood flow. An obvious drawback for this type of intervention is the extended recovery time due to the invasive nature of the procedure.

As well in the 1960s, Dotter [1, 3, 7, 14] pioneered catheter-based cardiovascular intervention as a means for less invasive procedures that could be performed with local anesthesia, resulting in much greater recovery times relative to open surgery. Advancement in catheter-based intervention came with the development of balloon angioplasty by Gruntzig et al. [5] in 1977. Balloon angioplasty involves inserting a balloon catheter into the damaged vessel and inflating the balloon to a fixed diameter by applying pressures that are on an order of magnitude of two times that of normal blood pressure [15]. After expansion of the stenotic vessel, the balloon is removed. Largely as a result of acute closure of the vessel, failure rates were as high as 50%. This was due to the mechanical properties of the arteries and the atherosclerotic plaques being relatively elastic, therefore returning to their original diameter after removal of the balloon [3]. As a result of the larger magnitude of the applied pressure compared to the normal pressure

exerted on the arterial wall, problems with tissue rupture occurred, which resulted in tissue flaps blocking the blood flow [3]. To prevent abrupt closure of the vessel and to tackle the problem with tissue flaps obstructing blood flow, stent technology was developed for use in tandem with angioplasty.

1.3 Cardiovascular Stents

Stents are tubular mechanical scaffolds that are implanted into stenotic vessels in order to re-open the vessel to restore blood flow. Although stents were actually under development in the 1960s, the first self-expanding bare metal stent (BMS) was implanted in a human by Sigwart et al. [5, 7, 14] in 1986. This was followed by the first implantation of a balloon-expandable stent in 1987 by Palmaz et al. [3, 5]. Self-expandable BMS are typically fabricated as wire meshes and are manufactured using nitinol (nickel-titanium alloy), due to the shape memory characteristics of nitinol. By designing the stent to have a relaxed diameter just greater than that of the vessel, they can be compressed into a catheter and once deployed at the treatment site, expand the stenotic vessel to restore blood flow. Palmaz et al. [3] fabricated balloon-expandable stents as thin-walled slotted tubes to be utilized as a scaffold incorporated with balloon angioplasty. These stents are typically manufactured with stainless steel or cobalt-chromium alloys.

Though the first stents were implanted in the 1980s, it wasn't until the early 1990s that stents entered the US market as the primary therapy to treat cardiovascular diseases. By the early 1990s, well over a million balloon dilations were performed with

over 600,000 per year being performed as of today in the coronary arteries alone [7]. As of 2008, there have been 21 balloon expandable stents and 28 self-expanding stents approved by the FDA for human use [3, 14].

The major design concept for the development of cardiovascular stents was to prevent post-traumatic vasospasm [7, 14]. Spasming of the vessels due to injury upon implantation leads to vasoconstriction, resulting in ischemia of the tissues downstream. In addition to the major design concept, stents also tackle injured flaps of the lumen preventing downstream embolic complications [7, 14]. Though the design seemed to be flawless with early results showing a decrease in cases of restenosis, two modes of chronic failure still exist with the implantation of stents [7, 14]. Acute thrombosis occurs immediately after deployment due to the natural foreign body response, though this is treatable with anticoagulant drug therapy [7, 14]. In addition, the most critical failure mode is in-stent restenosis. In-stent restenosis is caused due to the injury to the vessel lumen upon deployment, which leads to neointimal hyperplasia caused by the proliferation of smooth muscle cells. In 2010, it was reported that about 15% – 20% of all cases required patients to have re-intervention within 6 – 12 months after implantation of BMS [5]. Though restenosis occurs in both the coronary and peripheral arteries, there is a higher rate of occurrence in the peripheral arteries. This is due to the much harsher biomechanical environment in the peripheral arteries, which includes vessel deformations due to limb movement and slow and reversing flow, among other features [8].

Though design modifications to bare metal stents have been attempted to reduce the incidence of in-stent restenosis, marked reduction of in-stent restenosis was only achieved by the advent of stents carrying active pharmaceutical agents, called drug eluting stents (DES) [5]. DES are polymer coated metallic stents that contain active pharmaceutical agents that are released as the polymer degrades at the site of the foreign body implantation. Introduced in the European market in 2002, first generation DES revolutionized the management of coronary artery disease [5]. After approval for clinical use in the US in 2003, 35% of all stent implantations were DES, with this percentage increasing to 90% by 2006 [5]. Through the controlled release of high local concentrations of either antiproliferative or immunosuppressant drugs directly to the site of injury from implantation, DES greatly inhibited in-stent restenosis over BMS.

In the mid 1990s, heparin and dexamethasone were reported as pharmaceutical agents that showed success as local drug delivery in the cardiovascular system. The objective of pharmaceutical agents used in DES is to address a particular stage of the restenotic cascade: (i) heparin is loaded in the stent and delivered to the injured site to reduce thrombis formation, and (ii) dexamethalsone is delivered as a pharmaceutical agent to reduce inflammation [7]. Though these DES showed improvement in reducing in-stent restenosis, the most effective agents have proven to be antiproliferative agents, such as Paclitaxel and Sirolimus [7, 19]. Paclitaxel functions by inhibiting microtubule depolymerization, thus effecting cell division and migration. Sirolimus prevents the initiation of DNA synthesis by having an antiproliferative effect on vascular smooth muscle cells [7]. Good restenosis results have been presented by the randomized

RAVEL trials and follow-up SIRIUS studies with Sirolimus eluting stents, where zero restenosis in six months was observed in 238 patients, while the TAXUS series of randomized trials showed good restenosis results with Paclitaxel eluting stents [7]. Still problems are reported with the use of drug eluting stents. Incomplete endothelialization of the stent struts causes delayed stent thrombosis. In addition, limited data exist on the application of drug eluting stents in the peripheral arteries. Sirolimus eluting stents deployed in long lesions in the peripheral arteries in the SCIROCCO trials showed promising short-term results with 6% restenosis at six months, but no difference than bare metal stents beyond 18 months [7].

1.4 Biodegradable Stents

The next revolution in minimally invasive surgery to advance cardiovascular interventions is thought to be the development of fully biodegradable polymeric stents. Due to the aforementioned complications that arise as a result of the implantation of metallic stents, the development of fully biodegradable polymeric stents has gained popularity in the recent decade. In addition, theoretical concerns that exist with metallic stents include: (i) high thrombogenicity as a result of most metals being positively charged, (ii) a permanent metallic stent remaining in the vessel may interfere with future clinical procedures, as well as provide more surface area for thrombus formation, and (iii) metals are not a feasible material to act as loadable drug carriers due to their microstructural properties [14]. Each of these problems has led to significant efforts to develop new materials for stents.

Though no long-term conclusive data exists yet, it is generally thought that after cardiovascular intervention, mechanical support for stenotic vessels is only needed for six months until re-endothelialization and healing are obtained [12]. Beyond this time period, there has been no demonstration to show any advantageous purpose for the presence of a permanent stent [8, 12]. Potential advantages of biodegradable polymeric stents have been documented by various researchers. Rajagopal et al. [7, 8, 12, 14] stated there are at least three advantages to the development of a temporary stent: (i) by having a stent that degrades and is absorbed into the body, there will no longer be an obstacle for future treatments and there will not be a permanent potential nidus for infection, (ii) the gradual softening of the material would provide both a smooth transfer of the loading from the stent to the arterial wall and would contravene the difference in compliance between the stent and the arterial wall, and (iii) the size required of a polymeric stent would provide an appreciable reservoir for anti-proliferative drug incorporation, while its degradation would serve a function in optimal drug release kinetics. Zidar et al. [18] proposed the following characteristics for the ideal stent to have proper mechanical characteristics, as well as drug dispersion ability: (i) the stent should be biodegradable and after serving its purpose, the breakdown products must be biocompatible, (ii) the stent should possess physical properties, such as collapse pressure, in order to sufficiently perform it mechanical function, (iii) the stent should have sufficient longitudinal flexibility to facilitate insertion, and (iv) the stent should be able to deliver drugs locally to prevent in-stent restenosis.

Though there are benefits that encourage the development of biodegradable polymeric stents, drawbacks exist due the mechanical properties of polymers versus metallic materials. Typically, polymers are weaker than metals, so difficulty arises in ensuring that sufficient strength is there to re-open the vessels and alleviate symptoms acutely [8, 19]. As well and due to the degradation that is to occur, designing a stent that can maintain structural integrity for a predictable, appropriate time to facilitate artery healing is even more challenging [8]. In addition to maintaining proper structural properties, the design of a polymer that can expand and maintain its shape proves to be a problem. With both self-expanding and balloon-expanding metallic stents, this has not been an issue due to metals being elastic-plastic materials. Rather than the metallic stent undergoing elastic deformation, metallic stents typically undergo plastic deformation, so once the final shape is obtained, recoil is not quite as likely. Due to the viscoelastic nature of polymers, this is not necessarily feasible [4, 17].

To sum up major challenges that are encountered in design concepts of polymeric stents, the following are considered: (i) the selection of appropriate structural polymeric materials that must be both biodegradable and biocompatible, (ii) the development of a stent design that is adapted to the material properties of the polymer, and (iii) the identification of a stent expansion protocol adapted to the intended implantation site [4].

1.5 Research Objectives

There have been several analyses and designs of biodegradable polymeric stents, focusing mainly on elastic behaviors of the polymers. Polymers, including some available tests on biodegradable polymers, are shown to experience pronounced viscoelastic response. This study presents analyses of biodegradable viscoelastic polymeric stents under mechanical loadings. The first part considers a cylindrical annulus as an idealized and simplified model for stents, which is done in order to gain deep understanding on the performance of degrading viscoelastic materials with prescribed boundary conditions that mimic mechanical loading in stents. The second part includes two realistic tubular meshes of currently available stents, allowing examination of the effects of materials and geometries on the performance of degrading stents. For the current study, the deformations in the polymeric stents due to internal cyclic loading that is to represent an idealized blood pressure, coupled with a constant external pressure that is to mimic the arterial pressure exerted on the stent due to the artery resisting expansion, will be observed. In addition, strain-induced degradation will be incorporated once the observed critical strain has been reached in order to model mechanical degradation in the polymeric stents. A comparison of various degradation rates, representing slow and fast degradation processes, will be presented and how they vary at the outer and inner surfaces of the stents. To achieve this goal, the following tasks are performed.

i. Using mechanical properties obtained from previous experimental studies, develop a simplified stent model that consists of a cylindrical annulus. This

simplified model is utilized to focus on the linear viscoelastic solid-like response of a degrading polymer without inclusion of failure modes such as strut fracture.

ii. Develop a numerical algorithm assuming a homogeneous, linear, isotropic material. Using the state variable method suggested by Simo et al. [11, 21] to determine the stress response calculation of the convolution integral, incorporate the algorithm in a user-defined material (UMAT) subroutine to be implemented with the finite element software ABAQUS, available through Texas A&M University's supercomputing facility.

iii. Modify the stress response obtained in the numerical algorithm by modifying the time-dependent material properties so that the degradation will occur until the mechanical properties associated with the modulus of the polymers are 20% of their original value.

iv. Apply idealized loading conditions to the model, as well as appropriate boundary conditions to allow the model to compress under the loading. The internal pressure to mimic an idealized blood pressure is taken as $\frac{120 mmHg}{80 mmHg}$ and at a frequency of 1 Hz, simulating resting conditions. A constant pressure exerted to the outer surface of the model taken as 2 atm, simulating how the arterial wall will have a crushing effect on the stent.

The model presented for the majority of this study is simplified to focus strictly on the numerical algorithm and degradation function presented in Chapter II, in order to

examine the effect of viscoelastic material response in polymeric stents under the prescribed loading conditions. Further studies to examine the problem at hand should include non-linear and long-term responses to mimic the true nature of polymers. As well, temperature and concentration should be included in further models due to stents being deployed in aqueous environments inside the human body.

CHAPTER II

MATERIALS AND METHODS

2.1 Viscoelasticity

Polymers belong to a class of materials known as viscoelastic materials that exhibit both elastic and viscous characteristics when undergoing deformations. Because of the additional viscous characteristic that differs viscoelastic materials from elastic materials, viscoelastic materials exhibit a time or rate dependent response. Some phenomena that are observed in viscoelastic materials are: (i) under an input of constant strain, they exhibit stress relaxation, where the material will show a decrease in stress with time, (ii) upon an input of constant stress, they exhibit creep deformation, where the material will show an increase in strain with time, and (iii) the material will show hysteretic response when a cyclic loading is applied. In addition, stress-strain curves of viscoelastic materials differ from elastic materials in their response to loading and unloading cycles. Viscoelastic materials dissipate energy, which is converted into heat, whereas elastic materials do not. Hysteresis is observed in the stress-strain curves of viscoelastic materials, as seen in Figure 2.1, where the area inside the loop depicts the energy dissipation upon removal of the load.

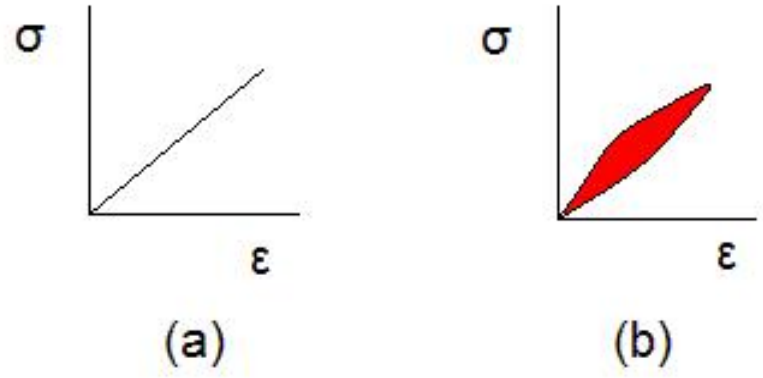

Figure 2.1: Stress-strain curves for (a) a purely elastic material and (b) a viscoelastic material. The red area is the hysteresis loop that depicts the amount of energy dissipated during a loading and unloading cycle. ***http://en.wikipedia.org/wiki/Viscoelasticity***

For polymers and other viscoelastic materials, the time-dependent material properties can be experimentally obtained through a few ways. Creep tests, stress relaxation tests, and dynamic mechanical analyses, where cyclic loads are applied over time, can be performed to determine the properties of viscoelastic materials. To express the viscoelastic nature of various materials, mechanical analogs can be constructed, in which springs and dashpots are arranged in ways that depict the deformation behavior due specific inputs. Springs and dashpots represent the elastic properties and the viscous properties of the material, respectively.

A mechanical analog known as the generalized Maxwell model, or Wiechert model, is depicted in Figure 2.2, which is used for modeling response of viscoelastic solid-like materials. In this mechanical analog, E_∞ represents the magnitude of the relaxation modulus when the material is fully relaxed. For each additional model, E_m and η_m represent the relaxation modulus and the viscosity coefficient for the m^{th} term. As will be mentioned in the development of a numerical algorithm, in order to calculate

the stress tensors at the current time, these additional models can be mathematically described using Prony series. Another model, which also describes the deformation of solid-like viscoelastic materials, is the generalized Kelvin-Voigt model, in which the springs and dashpots of the m^{th} models are connected in parallel, and then connected in series with a spring.

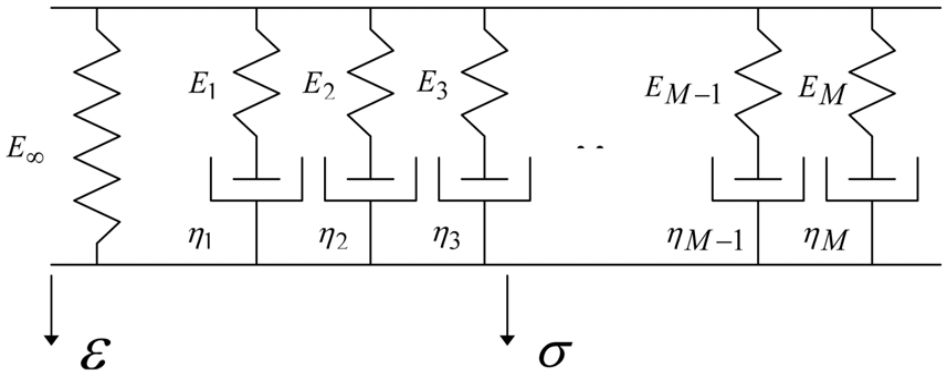

Figure 2.2: Generalized Maxwell model. Depicts the additional models that are mathematically expressed using Prony series [11].

2.2 Constitutive Model

Mathematically, the stress response of viscoelastic materials can be expressed using a convolution integral. For a one-dimensional model, the relaxation modulus for a viscoelastic material is used to define the stress response as a result of the input in strain history in terms of their respective tensor components [11, 21], which is:

$$\sigma(t) = \int_{0^-}^{t} E(t-s)\frac{d\varepsilon}{ds}ds \tag{2.1}$$

Because of the computational simplicity associated with exponential based functions, the time-dependent relaxation modulus within the integrand can be expressed by the use of Prony series. The relaxation modulus is then expressed as:

$$E(t) = E_{\infty} + \sum_{n=1}^{N} E_n e^{\frac{-t}{\tau_n}} \tag{2.2}$$

In Eq. (2.2), E_{∞} represents the long-term relaxation modulus when the material is fully relaxed and E_n and τ_n represent the relaxation modulus and relaxation time for each Prony term, respectively. The larger the value for the relaxation time, the slower the material will exhibit stress relaxation.

The one-dimensional model of the stress response due to a strain input can be expanded to three-dimensional for isotropic materials as seen in Eq. (2.3), which is associated to Lamé constants for linear elastic materials. In three dimensions, the constitutive relationship is often separated into two components: deviatoric and volumetric components. The shear components of the strain tensors are included in the calculation of the deviatoric component of the stress tensor. The volume change is determined by the normal components of the strain tensor. By rearranging components that correspond to the total strain and volumetric strain, the stress output is given in Eq. (2.3). Repeating indices, as seen in the second component of the stress tensor in Eq.

(2.3), depicts summations of the strain tensors. The Kronecker delta, δ_{ij}, is equal to 1 when the indices *i* and *j* are equal, and 0 when the indices are not equal.

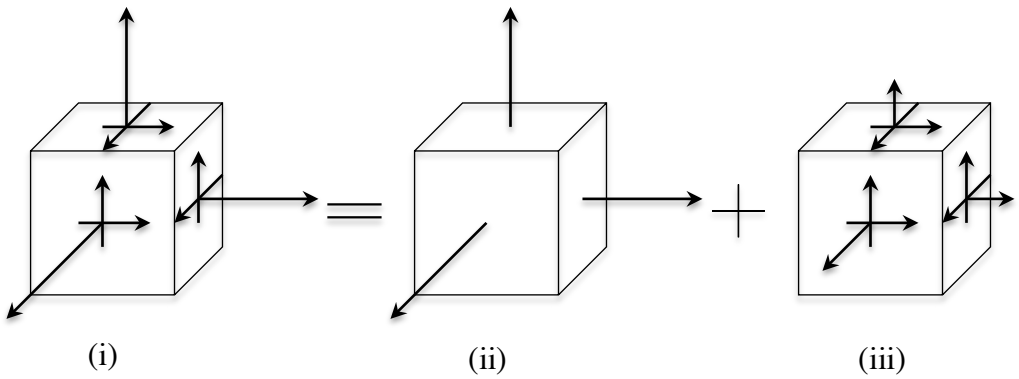

Figure 2.3: Decomposition of a general stress state (i) into a hydrostatic stress state (ii) and a deviatoric state [20].

$$\sigma_{ij}(t) = 2\int_{0^-}^{t} \mu(t-s)\frac{d\varepsilon_{ij}}{ds}ds + \delta_{ij}\int_{0^-}^{t} \lambda(t-s)\frac{d\varepsilon_{kk}}{ds}ds \tag{2.3}$$

In addition, as seen in Eq. (2.3), the convolution integral is modified when expanding into three dimensions by the introduction of the Lamé constants. The first Lamé constant, λ, is a function of the shear and bulk moduli. The second Lamé constant, μ, is represented as the shear modulus. These material properties are expressed mathematically by Eqs. (2.4) – (2.6). The shear modulus represents a materials resistance to distortion, or shape change, while the bulk modulus represents the materials resistance to volume change. If the corresponding Poisson's ratio, ν_0, is assumed to be

constant, the shear and bulk moduli have the same time-dependent behavior as the extensional relaxation modulus:

$$\lambda(t) = K(t) - \frac{2}{3}\mu(t) \tag{2.4}$$

$$\mu(t) = \frac{E(t)}{2(1+\upsilon_0)} \tag{2.5}$$

$$K(t) = \frac{E(t)}{3(1-2\upsilon_0)} \tag{2.6}$$

By modifying the convolution integral for a three-dimensional solid with Prony series, as was the case in the one-dimensional model, the time-dependent Lamé constants are expressed as seen in Eqs. (2.7) – (2.8).

$$\mu(t) = \mu_\infty + \sum_{n=1}^{N} \mu_n e^{\frac{-t}{\tau_n}} \tag{2.7}$$

$$\lambda(t) = \lambda_\infty + \sum_{n=1}^{N} \lambda_n e^{\frac{-t}{\tau_n}} \tag{2.8}$$

2.3 Numerical Algorithm

A numerical algorithm is presented to calculate the stress response due to a given strain input at the current time, which can be directly integrated to finite element model. Simo et al. suggested a state variable method for calculating the stress response of the

convolution integral [11, 21]. This numerical method uses the state variable, or history variable, from the stress calculation at increment n to obtain the stress calculation at increment n+1. The computational time is significantly reduced using this method as compared to other computational inefficient methods such as the piecewise method. In the piecewise method, every time step that precedes the time step of interest must be calculated, which proves to be inefficient for large amounts of data [11]. Using the state variable method, Muliana and Rajagopal [10] and Tscharnuter and Muliana [16] developed a numerical algorithm based on the quasi-linear viscoelastic model (QLV) presented by Fung in 1981 that has been found reasonably good in modeling moderate deformations in viscoelastic materials.

To develop the numerical algorithm for the time-dependent stress response at time t, the Prony series depicted in Eqs. (2.7) – (2.8) are substituted into the convolution integral for a three-dimensional solid in Eq. (2.3), which is:

$$\sigma_{ij}(t) = 2\int_{0^-}^{t}\left[\mu_\infty + \sum_{n=1}^{N}\mu_n e^{\frac{-(t-s)}{\tau_n}}\right]\frac{d\varepsilon_{ij}}{ds}ds + \delta_{ij}\int_{0^-}^{t}\left[\lambda_\infty + \sum_{n=1}^{N}\lambda_n e^{\frac{-(t-s)}{\tau_n}}\right]\frac{d\varepsilon_{kk}}{ds}ds \tag{2.9}$$

The long-term component as time goes to infinity and the summation components of the Prony series in each integral are separated, and keeping in mind that the strain input is zero at time t=0, the stress response is simplified as seen in Eq. (2.10). Note that the Lamé constants for each n^{th} model are left inside the integral. This will be shown to come into play in the incremental form of the time-dependent stress response

at time t, and differs from the state variable method presented by Simo et al. [11, 21], in which the constants are pulled out of the integral.

$$\sigma_{ij}(t) = 2\left[\mu_\infty \varepsilon_{ij}(t) + \sum_{n=1}^{N} \int_{0^-}^{t} \mu_n e^{\frac{-(t-s)}{\tau_n}} \frac{d\varepsilon_{ij}}{ds} ds\right] + \delta_{ij}\left[\lambda_\infty \varepsilon_{kk}(t) + \sum_{n=1}^{N} \int_{0^-}^{t} \lambda_n e^{\frac{-(t-s)}{\tau_n}} \frac{d\varepsilon_{kk}}{ds} ds\right] \tag{2.10}$$

Now, the integrals inside of the summations can be expressed using the introduction of state variables. This is shown in Eq. (2.11), followed by the calculation of the state variables at the current time in Eqs. (2.12) – (2.15).

$$\sigma_{ij}(t) = 2\left[\mu_\infty \varepsilon_{ij}(t) + \sum_{n=1}^{N} q_{ij}^{n,t}\right] + \delta_{ij}\left[\lambda_\infty \varepsilon_{kk}(t) + \sum_{n=1}^{N} q_{kk}^{n,t}\right] \tag{2.11}$$

The description for the state variables is given in Eqs. (2.12) – (2.13). This allows for the state variable from the previous increment to be used in the calculation for the state variable at the current increment. The first integral is modified by the addition of $-\Delta t + \Delta t$ into the exponential. By doing so, the exponential $e^{\frac{-\Delta t}{\tau_n}}$ can be pulled out of the integral, yielding the same integral form of the state variables represented in Eqs. (2.10) – (2.11). This new integral is defined as the state variable from the previous increment.

$$q_{ij}^{n,t} = \int_{0^-}^{t-\Delta t} \mu_n e^{\frac{-(t-s-\Delta t+\Delta t)}{\tau_n}} \frac{d\varepsilon_{ij}}{ds} ds + \int_{t-\Delta t}^{t} \mu_n e^{\frac{-(t-s)}{\tau_n}} \frac{d\varepsilon_{ij}}{ds} ds \tag{2.12}$$

$$q_{kk}^{n,t} = \int_{0^-}^{t-\Delta t} \lambda_n e^{\frac{-(t-s-\Delta t+\Delta t)}{\tau_n}} \frac{d\varepsilon_{kk}}{ds} ds + \int_{t-\Delta t}^{t} \lambda_n e^{\frac{-(t-s)}{\tau_n}} \frac{d\varepsilon_{kk}}{ds} ds \tag{2.13}$$

The second integral is evaluated using the trapezoidal rule. The final form for the calculation of the state variables at the current increment is depicted in Eqs. (2.14) – (2.15). By substituting the state variables in Eqs. (2.14) – (2.15) into the equation for the stress tensors at the current time in Eq. (2.11), the final form for the stress response is seen in Eq. (2.16).

$$q_{ij}^{n,t} = e^{\frac{-\Delta t}{\tau_n}} q_{ij}^{n,t-\Delta t} + \mu_n \frac{\Delta t}{2} \left[\left. \frac{\Delta \varepsilon_{ij}}{\Delta t} \right|_t + e^{\frac{-\Delta t}{\tau_n}} \left. \frac{\Delta \varepsilon_{ij}}{\Delta t} \right|_{t-\Delta t} \right] \tag{2.14}$$

$$q_{kk}^{n,t} = e^{\frac{-\Delta t}{\tau_n}} q_{kk}^{n,t-\Delta t} + \lambda_n \frac{\Delta t}{2} \left[\left. \frac{\Delta \varepsilon_{kk}}{\Delta t} \right|_t + e^{\frac{-\Delta t}{\tau_n}} \left. \frac{\Delta \varepsilon_{kk}}{\Delta t} \right|_{t-\Delta t} \right] \tag{2.15}$$

$$\sigma_{ij}(t) = 2\left\{ \mu_\infty \varepsilon_{ij}(t) + \sum_{n=1}^{N} \left(e^{\frac{-\Delta t}{\tau_n}} q_{ij}^{n,t-\Delta t} + \mu_n \frac{\Delta t}{2} \left[\left. \frac{\Delta \varepsilon_{ij}}{\Delta t} \right|_t + e^{\frac{-\Delta t}{\tau_n}} \left. \frac{\Delta \varepsilon_{ij}}{\Delta t} \right|_{t-\Delta t} \right] \right) \right\}$$

$$+\delta_{ij} \left\{ \lambda_\infty \varepsilon_{kk}(t) + \sum_{n=1}^{N} \left(e^{\frac{-\Delta t}{\tau_n}} q_{kk}^{n,t-\Delta t} + \lambda_n \frac{\Delta t}{2} \left[\left. \frac{\Delta \varepsilon_{kk}}{\Delta t} \right|_t + e^{\frac{-\Delta t}{\tau_n}} \left. \frac{\Delta \varepsilon_{kk}}{\Delta t} \right|_{t-\Delta t} \right] \right) \right\} \tag{2.16}$$

To implement the constitutive equation derived above in ABAQUS through the use of a UMAT subroutine, the incremental form of the stress tensors is derived. The

description of the incremental stresses is seen in Eq. (2.17), whereas the final incremental form of the stress tensors is shown in Eq. (2.18).

$$\Delta\sigma_{ij}^{t} = \sigma_{ij}^{t} - \sigma_{ij}^{t-\Delta t} \tag{2.17}$$

$$\Delta\sigma_{ij}^{t} = 2\mu_{\infty}\Delta\varepsilon_{ij}^{t} + \delta_{ij}\lambda_{\infty}\Delta\varepsilon_{kk}^{t} + 2\sum_{n=1}^{N}\left\{ q_{ij}^{n,t-\Delta t}\left(e^{\frac{-\Delta t}{\tau_n}} - 1 \right) + \mu_n \frac{\Delta t}{2}\left[\left.\frac{\Delta\varepsilon_{ij}}{\Delta t}\right|_{t} + e^{\frac{-\Delta t}{\tau_n}} \left.\frac{\Delta\varepsilon_{ij}}{\Delta t}\right|_{t-\Delta t} \right] \right\}$$

$$+\delta_{ij}\sum_{n=1}^{N}\left\{ q_{kk}^{n,t-\Delta t}\left(e^{\frac{-\Delta t}{\tau_n}} - 1 \right) + \lambda_n \frac{\Delta t}{2}\left[\left.\frac{\Delta\varepsilon_{kk}}{\Delta t}\right|_{t} + e^{\frac{-\Delta t}{\tau_n}} \left.\frac{\Delta\varepsilon_{kk}}{\Delta t}\right|_{t-\Delta t} \right] \right\} \tag{2.18}$$

In addition to the incremental stress tensors, it is necessary to determine the consistent tangent modulus, at each material point at each instant of time. This is accomplished by performing the partial derivatives seen in Eq. (2.19). Eqs. (2.20) – (2.22) depict the definition for the components of the consistent tangent modulus. For an isotropic material, the components of the consistent tangent modulus not depicted are zero.

$$C_T = \frac{\partial\Delta\sigma_{ij}^{t}}{\partial\Delta\varepsilon_{ij}^{t}} \tag{2.19}$$

$$\frac{\partial\Delta\sigma_{11}^{t}}{\partial\Delta\varepsilon_{11}^{t}} = \frac{\partial\Delta\sigma_{22}^{t}}{\partial\Delta\varepsilon_{22}^{t}} = \frac{\partial\Delta\sigma_{33}^{t}}{\partial\Delta\varepsilon_{33}^{t}} = 2\mu_{\infty} + \lambda_{\infty} + \sum_{n=1}^{N}\mu_n + \frac{1}{2}\sum_{n=1}^{N}\lambda_n \tag{2.20}$$

$$\frac{\partial\Delta\sigma_{11}^{t}}{\partial\Delta\varepsilon_{22}^{t}} = \frac{\partial\Delta\sigma_{22}^{t}}{\partial\Delta\varepsilon_{33}^{t}} = \frac{\partial\Delta\sigma_{22}^{t}}{\partial\Delta\varepsilon_{11}^{t}} = \frac{\partial\Delta\sigma_{22}^{t}}{\partial\Delta\varepsilon_{33}^{t}} = \frac{\partial\Delta\sigma_{33}^{t}}{\partial\Delta\varepsilon_{11}^{t}} = \frac{\partial\Delta\sigma_{33}^{t}}{\partial\Delta\varepsilon_{22}^{t}} = \lambda_{\infty} + \frac{1}{2}\sum_{n=1}^{N}\lambda_n \tag{2.21}$$

$$\frac{\partial \Delta\sigma_{12}^{t}}{\partial \Delta\gamma_{12}^{t}} = \frac{\partial \Delta\sigma_{13}^{t}}{\partial \Delta\gamma_{13}^{t}} = \frac{\partial \Delta\sigma_{23}^{t}}{\partial \Delta\gamma_{23}^{t}} = \mu_{\infty} + \frac{1}{2}\sum_{n=1}^{N}\mu_{n} \tag{2.22}$$

2.4 Model of Degradation

Environmental factors have an effect over long-term performance of polymers. Temperature, humidity, and concentration (if the material is submerged in an aqueous environment) affect the deformation of polymers, among other factors. In biodegradable polymers, the degradation occurs via hydrolysis process and the existence of mechanical stress/strain accelerates the degradation in the polymers, as experimentally shown by Soares [14]. To simplify the model for the current study, the degradation function is modeled as strain-induced only. The material will respond in the manner defined by the constitutive relationship derived in the previous section until a threshold strain is reached. Beyond this point, the material will degrade in the fashion described below. As the material degrades, it is expected that the material properties such as the modulus will decrease. The rate of degradation, as seen in Eq. (2.23), is determined by the degradation at the current time and a function of the current magnitude of the strain vector, as previously studied by Soares et al. [12, 13] and Muliana and Rajagopal [10].

$$\dot{d} = (1-d) f(\underset{\sim}{\varepsilon}) \tag{2.23}$$

The function that determines how fast or slow the degradation will occur, $f(\underset{\sim}{\varepsilon})$, is defined in Eq. (2.24). The constant in the function, A, is the parameter that is adjusted

in order to affect the rate of degradation, as seen in Eq. (2.24). The larger the value for A, the faster degradation occurs. To determine when degradation is to onset, the threshold is compared with the norm of the strain tensor. This is depicted in Eqs. (2.25) – (2.27), where Eq. (2.27) gives the parameters at which degradation will occur.

$$f(\underset{\sim}{\varepsilon}) = A\bar{\varepsilon} \tag{2.24}$$

$$\bar{\varepsilon} = \left|\left|\underset{\sim}{\varepsilon}\right|\right| \tag{2.25}$$

$$\left|\left|\underset{\sim}{\varepsilon}\right|\right| = \sqrt{\varepsilon_{11}^2 + \varepsilon_{22}^2 + \varepsilon_{33}^2 + 2\varepsilon_{12}^2 + 2\varepsilon_{13}^2 + 2\varepsilon_{23}^2} \tag{2.26}$$

$$f(\underset{\sim}{\varepsilon}) = \begin{cases} 0 & \left|\left|\underset{\sim}{\varepsilon}\right|\right| \le \varepsilon_{cr} \\ A\left|\left|\underset{\sim}{\varepsilon}\right|\right| & \left|\left|\underset{\sim}{\varepsilon}\right|\right| > \varepsilon_{cr} \end{cases} \tag{2.27}$$

Though the above magnitude of the strain tensor is used in this study to define when degradation will onset, for future studies, it would be beneficial to define this value utilizing the square root of the second invariant (J_2), ensuring that the values remain the same regardless of coordinate transformation. Therefore, degradation would onset when $\left|\left|J_2\right|\right| > \varepsilon_{cr}$. The second strain invariant is defined in Eq. (2.28) and in tensor notation in Eq. (2.29).

$$J_2 = \varepsilon_{11}\varepsilon_{22} + \varepsilon_{22}\varepsilon_{33} + \varepsilon_{33}\varepsilon_{11} - \varepsilon_{12}^2 - \varepsilon_{13}^2 - \varepsilon_{23}^2 \tag{2.28}$$

$$J_2 = \frac{1}{2}\left[\varepsilon_{kk}\varepsilon_{mm} - \varepsilon_{ij}\varepsilon_{ij}\right] \tag{2.29}$$

To solve for the degradation at the current time, a relationship for the rate of degradation is introduced in Eq. (2.28). By replacing this relationship for the rate of degradation in Eq. (2.23), the degradation at the current time can be defined as seen in Eq. (2.29).

$$\dot{d} = \frac{dd}{dt} \cong \frac{d^{t+\Delta t} - d^{t}}{\Delta t} \cong \frac{d^{t} - d^{t-\Delta t}}{\Delta t} \tag{2.30}$$

$$d^{t} = \frac{\Delta t \cdot f(\underset{\sim}{\varepsilon}^{t}) + d^{t-\Delta t}}{(1 + \Delta t \cdot f(\underset{\sim}{\varepsilon}^{t}))} \tag{2.31}$$

Now that the degradation at the current time is defined, Eqs. (2.30) – (2.31) show how the relaxation modulus is now modified to enable degradation once the critical strain is surpassed. The constant alpha, α , in Eqs. (2.30) – (2.31) is taken to be 0.8. This is to prescribe a condition that the material will degrade to a point at which the material properties are 20% of their original values.

$$E_{\infty} = E_{\infty}(1 - \alpha d^{t}) \tag{2.32}$$

$$E_{n} = E_{n}(1 - \alpha d^{t}) \tag{2.33}$$

2.5 Material Parameters

Rather than using typical stent geometry for this study, a simplified model consisting of a cylindrical annulus was first used. The parameters for this model were

determined using the average dimensions of a human coronary artery. With an average diameter of 5 mm for a human coronary artery, the outer dimension of the cylindrical annulus was taken to be 5 mm. Assuming that the typical strut thickness for a stent is 100 μm, this yields an inner radius for the model to be 2.4 mm. The length of the model was taken to be 20 mm, a typical length for stents in use today. Because of symmetry about each axis, only half of the length and one-fourth of the circumference are needed. This is depicted in Figure 2.4.

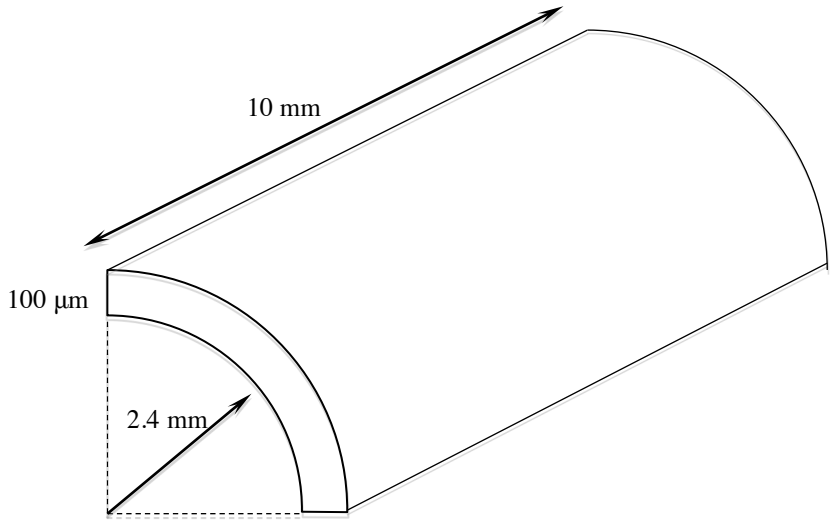

Figure 2.4: Dimensioned cylindrical annulus utilized to simulate a cardiovascular stent.

Roller boundary conditions were applied to the symmetry planes to allow the material model to compress or expand in the radial direction. The positive y-axis is into the page, as seen in Figure 2.5. To simulate a stent deployed in a human coronary artery, two pressures are applied. To simulate the loading on the stent due to the pulsatile blood

flow within the artery, and ideal blood pressure for a healthy adult of $\frac{120 mmHg}{80 mmHg}$ was applied. This was accomplished my applying two separate loads to the inner surface. A constant component of 100 mmHg was superimposed with a sinusoidal pressure of 20 mmHg. The sinusoidal pressure was applied at a frequency of 1 Hz, to mimic a resting heart rate of 60 beats per minute. To model the pressure exerted on the stent by the arterial wall's resistance to expansion as a result of the inflation of the deployed stent, a constant pressure of 2 atm was applied to the external surface. All pressure units were converted to MPa to ensure consistency, thus are as follows: constant arterial pressure (0.20265 MPa), constant component of blood pressure (0.01333 MPa), and oscillatory component of blood pressure (0.00267 MPa).

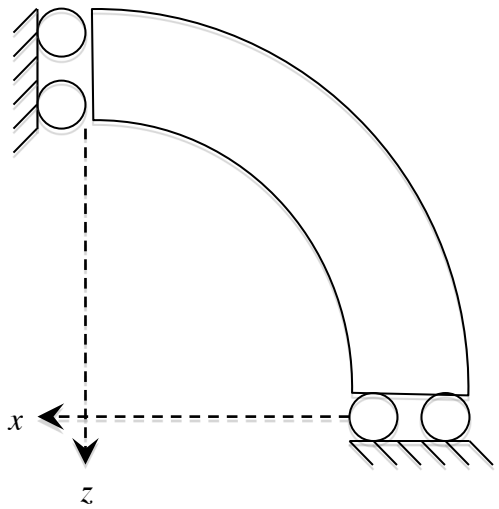

Figure 2.5: Roller boundary conditions applied to stent model.

Material properties for the stent were taken from literature regarding various polymers. Poly-L-lactic acid (PLLA) is a polymer commonly used in biomedical applications due to its biocompatibility. Soares [14] determined the time-dependent properties for PLLA for relatively short duration (10 minutes), as listed in Table 2.1. In addition to PLLA, material properties for polyoxymethylene (POM) were also considered. Time-dependent mechanical properties for POM under relatively long duration (40,000 minutes) are listed in Table 2.2. POM is a polymer commonly used in applications such as gears, springs, and hinges, but is used in a comparative study in this case to see how different polymers degrade and deform under the same loading conditions. In the tables, K_n refers to the normalized time-dependent function for each Prony series, and is defined as $K(t) = \frac{E(t)}{E(0)}$. For the assignment of mechanical properties in each ABAQUS input file, the instantaneous elastic modulus for each polymer is multiplied by each n^{th} normalized time-dependent function. The instantaneous modulus is multiplied by the top row in each table to determine the modulus in the fully relaxed states. Taken from a number of literature sources, the elastic modulus for PLLA is assumed to be 2.0 GPa. The relaxation time for each Prony series is represented by τ_n. In addition, the material is assumed to be nearly incompressible, thus having an assigned Poisson's ratio of 0.45.

Table 2.1: Time-dependent data for PLLA.

n	K_n	τ_n (sec)
~	0.68259	~
1	0.17659	11.852
2	0.13882	198.56

A.Muliana, K.R. Rajagopal / International Journal of Solids and Structures 49 (2012) 989-1000

Table 2.2: Time-dependent data for POM.

n	K_n	τ_n (sec)
~	0.47271	~
1	0.04513	19.11205
2	0.0679	140.8967
3	0.06122	965.5306
4	0.06205	8385.041
5	0.07	20000
6	0.071	70000
7	0.06	120000
8	0.05	500000
9	0.04	1500000

D. Tscharnuter, A. Muliana / Polymer 54 (2013) 1208-1217

CHAPTER III

PRELIMINARY TESTING

3.1 UMAT Implementation

To simulate the loading that a typical stent is subjected to upon deployment, the commercial finite element software ABAQUS/CAE available through Texas A&M University's supercomputing facility was utilized. In addition, the material models were defined and implemented through a user-defined material subroutine (UMAT). The UMAT subroutine is a tool that allows the user to define the mechanical constitutive relations of a given material. FORTRAN syntax is used to develop the UMAT code.

Variables that are known at the current time for each increment are $\varepsilon_{ij}^{t-\Delta t}$, $\Delta\varepsilon_{ij}^{t}$, $\sigma_{ij}^{t-\Delta t}$, and $q_{ij,kk}^{t-\Delta t}$. These variables refer to the strain tensor components at the previous time increment, the strain increment between the current and previous time steps, the stress tensor components at the previous time increment, and the history/state variables from the previous increment. The subscripts refer to the indices of the six components of the respective tensors, whereas the superscripts refer to the previous or current time step.

To define the material's mechanical constitutive relationship, the stress tensor at the current time step, along with the consistent tangent modulus and history/state variables must be calculated. These are σ_{ij}^{t}, C_T^t, and $q_{ij,kk}^{t}$, respectively. Because the loading prescribed is applied incrementally, the incremental stresses are calculated first from Eq. (2.18) and then the total stresses can be determined. Once σ_{ij}^{t} is calculated, C_T^t

is determined by taking the partial derivatives of the stress tensors over the strain tensors at the current time, which was discussed in Chapter II. The state variables are then updated at the current time and passed back into the code for the new values at the next increment. The algorithm for the UMAT code is presented in Figure 3.1, with the step-by-step procedure outlined below. An example of the UMAT code and an example input file are presented in Appendices A and B, respectively.

i. ABAQUS inputs the strain tensors at the previous time, the strain increment and the current time, the stress tensors at the previous time, and the time step.

ii. For the first increment, the state variables are initialized with a zero value. The subsequent state variables take on the value calculated at the end of the code.

iii. Calculate the norm of the current strain tensor. If the value is less than the critical strain, the scalar degradation variable has a zero value and the moduli remain the same. If it is greater, the degradation variable is calculated as presented in Chapter II, yielding new values for the moduli.

iv. Update the stresses and calculate the consistent tangent modulus as presented in Chapter II. The stresses calculated are in incremental form and summed with the stresses from the previous increment.

v. Calculate the new state variables to be passed back into the code at the beginning.

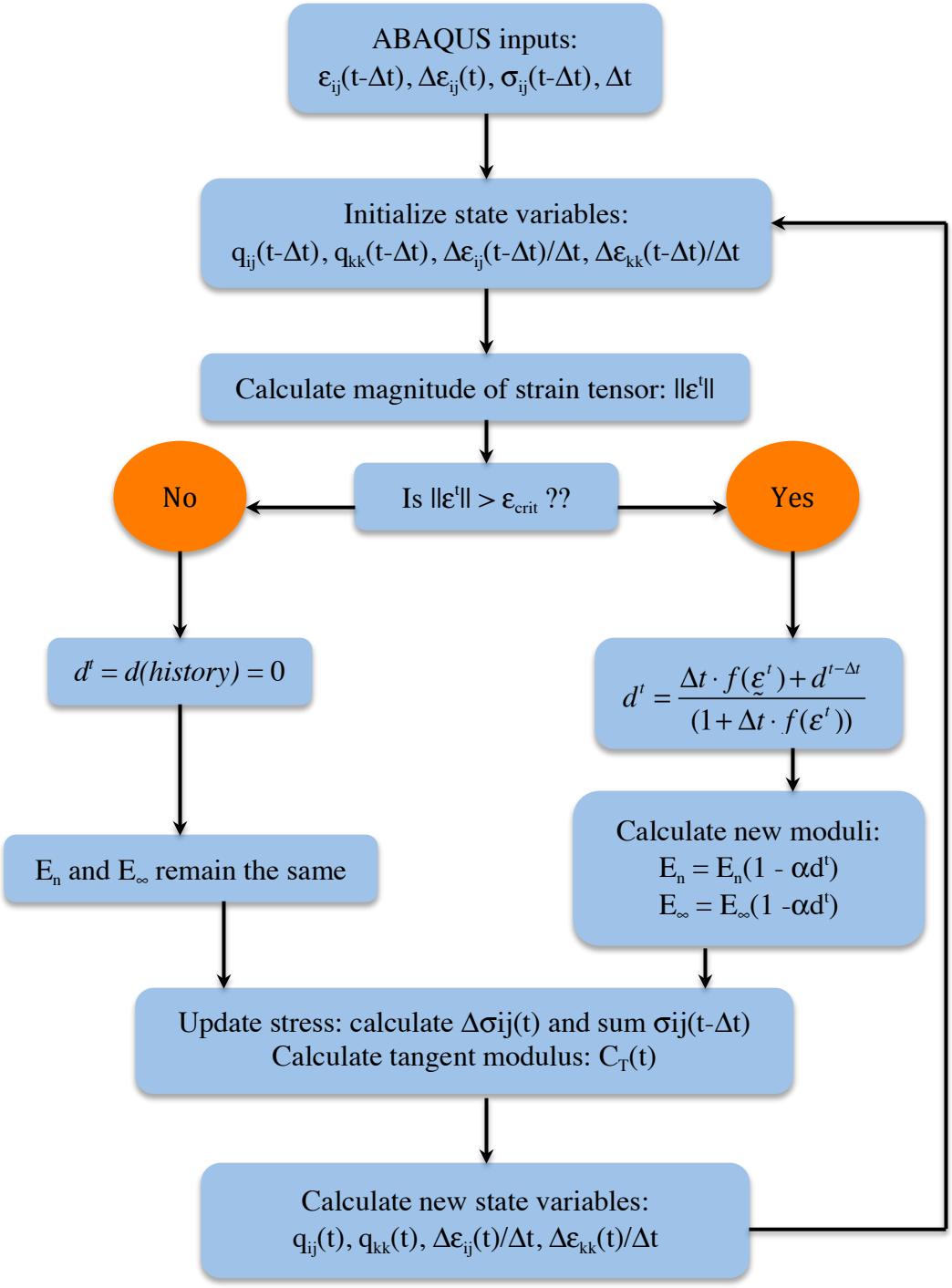

Figure 3.1: UMAT loop.

3.2 Single Element Test

Validation and verification of the UMAT code is needed to confirm that the results obtained from the simulations are indeed good approximations. To accomplish this task, a preliminary single element test was performed in order to simulate responses under uniform loading conditions, and compare the results with those of the analytical solutions. In addition to verifying the validity of the UMAT code, the single element test was utilized to determine the critical strain for each material model. Proper boundary conditions were applied to the surfaces of the element in order to simulate a uniaxial extensional loading. A uniform ramped extensional loading to yield an applied pressure of 20 MPa was applied to the four nodes on the positive yz-plane. The analysis was conducted for both viscoelastic materials (PLLA and POM), as well as a comparison with a linear elastic solid.

To verify that the viscoelastic effects provided by the longer time duration (with additional time-dependent Prony series) do indeed modify how the material deforms, the viscoelastic effect in the UMAT code was negated and compared with a response for an elastic solid, which is depicted in Figure 3.2. In this study, the instantaneous modulus for each material is the same, 2 GPa. The viscoelastic UMAT was compared with results obtained from both an elastic UMAT and a material assigned elastic properties within ABAQUS/CAE. As can be seen, the curves are exactly the same, thus verifying that the additional time-dependent Prony series in the viscoelastic UMAT do have an effect when not negated.

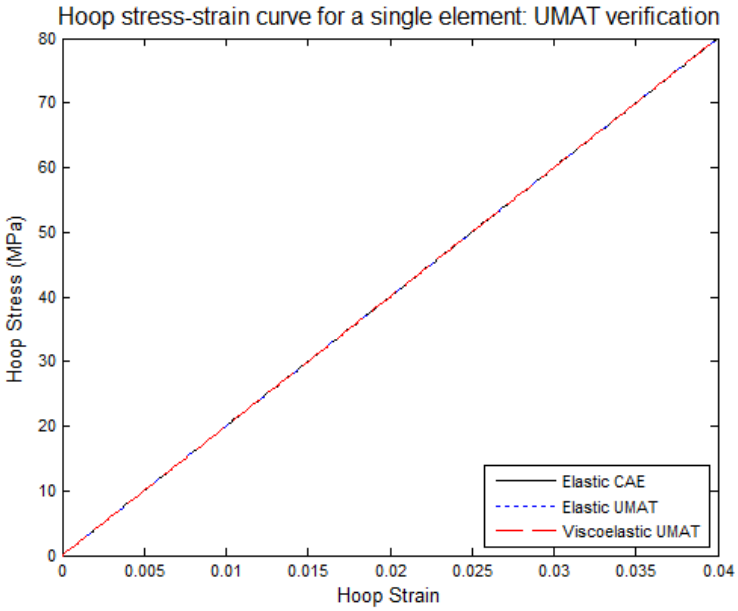

Figure 3.2: UMAT verification for the linear viscoelastic model. Compared with an elastic UMAT as well as elastic material model defined within ABAQUS/CAE.

From various literature sources, the tensile strength of PLLA is presented to be 45 MPa. The same tensile strength was assumed for POM for comparative studies, thus the only difference in the two material models is the time-dependent properties. Material properties applied to each single element model are presented in Tables 2.1 and 2.2. The extensional loading was applied linearly over 30 seconds. Results from the single element test yield the critical strains for PLLA and POM to be 2.47% and 2.30%, respectively. These results can be observed by the uniaxial stress-strain comparison of PLLA and POM presented in Figure 3.3. It is noted that for design purposes, it might be necessary to consider a lower value of critical stress/strain in order not to utilize the maximum capacity of the material. Alternatively, one can include a 'safety factor' in order to utilize only fractions of the maximum load carrying capacity of the material.

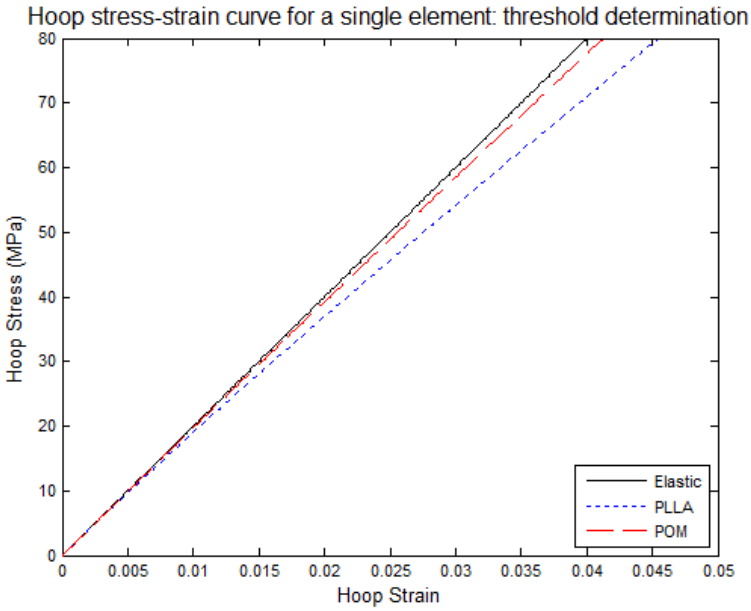

Figure 3.3: Stress-strain comparison for single element test of PLLA and POM at loading duration of 30 seconds. Also included is the stress-strain response for an elastic material with the same instantaneous modulus.

To verify that the UMAT code produces reasonably good results, a linearly increasing uniaxial strain was applied to the element. A 3% strain was applied over 10 seconds at a time increment of 0.1 seconds, yielding 100 increments. To test the degradation function in the UMAT code, the critical strain was modified so that degradation onsets during the 99th increment. This was done so that the degradation function at time $t - \Delta t$ in the stress calculation in last increment has a non-zero value, in order to check if the degradation is updating with each increment. To check the update of stresses, the first two increments are presented. The constant, A, in the degradation function in Eq. (2.24) was taken as 0.5. The corresponding stress at the final increment and the degradation functions for the final two increments were determined as are shown in Figure 3.4.

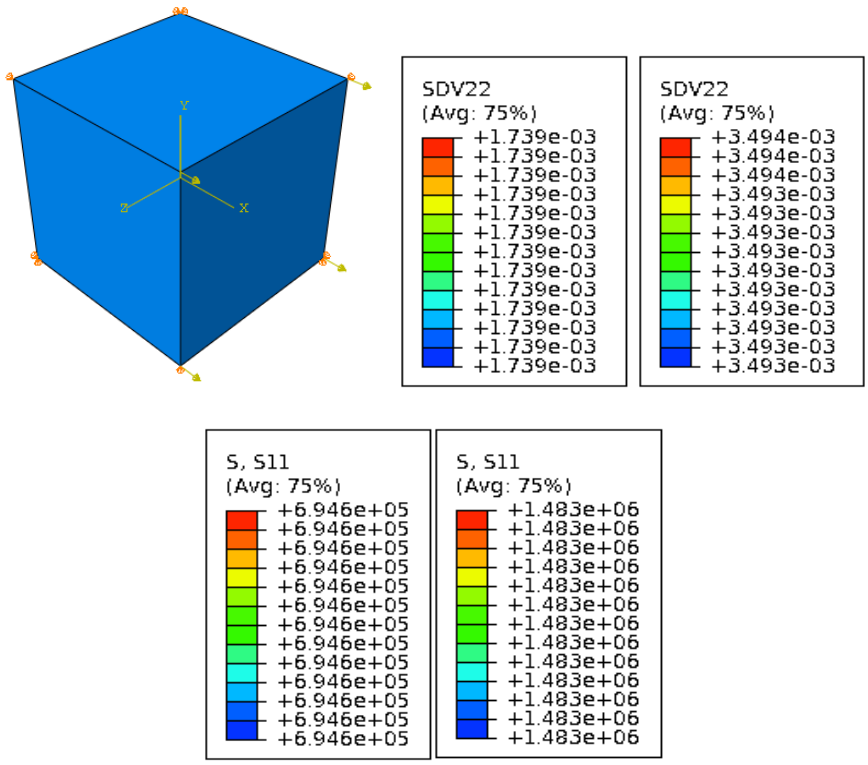

Figure 3.4: Degradation due to applied ramped uniaxial 3% strain. Top row left to right: single element model with applied strain in x-direction, degradation (SDV) at increment 99, degradation at increment 100. Bottom row left to right: stress (S11) at increment 1, stress at increment 2 (units in Pa).

The numerical results were compared with analytical results. Because the state variable method is used to obtain the stresses at the current time t, the task of determining the degradation simply involved substituting the known strains and material properties due to degradation from the last two increments into the degradation function derived in Chapter II. Eqs. (3.1) – (3.8) show the analytical results for the degradation at the final two increments, which are very close to the values determined from the numerical method (see Fig. 3.3). Eqs. (3.9) – (3.20) show the analytical results for the stress at the first two increments. As seen in Eqs. (3.9) – (3.12), the state variables have an initial value of zero at the first increment, making the stress calculation very simple.

Taking the calculated values of $q_{ij}^{n,t}$ and $q_{kk}^{n,t}$ from the first increment and substituting into $q_{ij}^{n,t-\Delta t}$ and $q_{kk}^{n,t-\Delta t}$ at the second increment, the stress at the second increment can be determined. The results can be compared with the numerical results in Figure 3.4.

Degradation at increment 99:

$$\varepsilon_1 = 0.0297 \tag{3.1}$$

$$\varepsilon_2 = \varepsilon_3 = \upsilon_0 \varepsilon_1 = 0.013365 \tag{3.2}$$

$$\left\| \underset{\sim}{\varepsilon}^t \right\| = \sqrt{\varepsilon_1^2 + \varepsilon_2^2 + \varepsilon_3^2} = \sqrt{0.001239} \tag{3.3}$$

$$d^{9.9} = \frac{\Delta t \cdot A \left\| \underset{\sim}{\varepsilon}^{9.9} \right\| + d^{9.8}}{1 + \Delta t \cdot A \left\| \underset{\sim}{\varepsilon}^{9.9} \right\|} = \frac{0.1 \cdot \left[0.5\sqrt{0.001239} \right] + 0}{1 + 0.1 \cdot \left[0.5\sqrt{0.001239} \right]} = 1.76E-3 \tag{3.4}$$

Degradation at increment 100:

$$\varepsilon_1 = 0.03 \tag{3.5}$$

$$\varepsilon_2 = \varepsilon_3 = \nu_0 \varepsilon_1 = 0.0135 \tag{3.6}$$

$$\left\| \underset{\sim}{\varepsilon}^t \right\| = \sqrt{\varepsilon_1^2 + \varepsilon_2^2 + \varepsilon_3^2} = \sqrt{0.0012645} \tag{3.7}$$

$$d^{10.0} = \frac{\Delta t \cdot A \left\| \underset{\sim}{\varepsilon}^{10.0} \right\| + d^{9.9}}{1 + \Delta t \cdot A \left\| \underset{\sim}{\varepsilon}^{10.0} \right\|} = \frac{0.1 \cdot \left[0.5\sqrt{0.0012645} \right] + 1.76E-3}{1 + 0.1 \cdot \left[0.5\sqrt{0.0012645} \right]} = 3.53E-3 \tag{3.8}$$

Stress at increment 1:

$$q_{ij}^{n,t-\Delta t} = q_{11}^{1,0} = q_{11}^{2,0} = 0 \tag{3.9}$$

$$q_{kk}^{n,t-\Delta t} = q_{11+22+33}^{1,0} = q_{11+22+33}^{2,0} = 0 \tag{3.10}$$

$$\left.\frac{\Delta\varepsilon_{ij}}{\Delta t}\right|_{t-\Delta t} = \left.\frac{\Delta\varepsilon_{11}}{\Delta t}\right|_{0} = 0 \tag{3.11}$$

$$\left.\frac{\Delta\varepsilon_{kk}}{\Delta t}\right|_{t-\Delta t} = \left.\frac{\Delta\varepsilon_{11+22+33}}{\Delta t}\right|_{0} = 0 \tag{3.12}$$

$$\sigma_{ij}(0.1) = 694623Pa \tag{3.13}$$

Stress at increment 2:

$$q_{ij}^{n,t-\Delta t} = q_{11}^{1,0.1} = 18268 \tag{3.14}$$

$$q_{ij}^{n,t-\Delta t} = q_{11}^{2,0.1} = 14361 \tag{3.15}$$

$$q_{kk}^{n,t-\Delta t} = q_{11+22+33}^{1,0.1} = 16441 \tag{3.16}$$

$$q_{kk}^{n,t-\Delta t} = q_{11+22+33}^{2,0.1} = 12925 \tag{3.17}$$

$$\left.\frac{\Delta\varepsilon_{ij}}{\Delta t}\right|_{t-\Delta t} = \left.\frac{\Delta\varepsilon_{11}}{\Delta t}\right|_{0.1} = 0.0003 \tag{3.18}$$

$$\left.\frac{\Delta\varepsilon_{kk}}{\Delta t}\right|_{t-\Delta t} = \left.\frac{\Delta\varepsilon_{11+22+33}}{\Delta t}\right|_{0.1} = 0.00003 \tag{3.19}$$

$$\sigma_{ij}(0.2) = 1431251Pa \tag{3.20}$$

3.3 Convergence Test

A mesh convergence test was performed to determine the proper element size needed to ensure reasonably accurate results of the tubular stents, as well as to maintain computational efficiency. The mesh in each separate study was generated using eight-node linear brick elements (C3D8) with each study refining from very coarse elements to very fine elements. The convergence study was performed using the material properties of PLLA presented in Table 2.1. A constant pressure of 3 MPa, which corresponds to 1 atm pressure, was applied to the external surface for a period of 25 seconds at a time increment of 0.05 seconds. The magnitude of the applied pressure was ramped from the value utilized to mimic the crushing pressure from the arterial wall for the purpose of ensuring that strain-induced degradation would occur in such a small time frame. The maximum hoop strain that occurs at the inner surface was then plotted as the number of elements in the model was increased. Figure 3.5 depicts the hoop strain over the number of elements for a slow degrading material model. As seen in Figure 3.5, the difference in strain from 4000 elements to 8000 elements is less than one-hundredth of a percent.

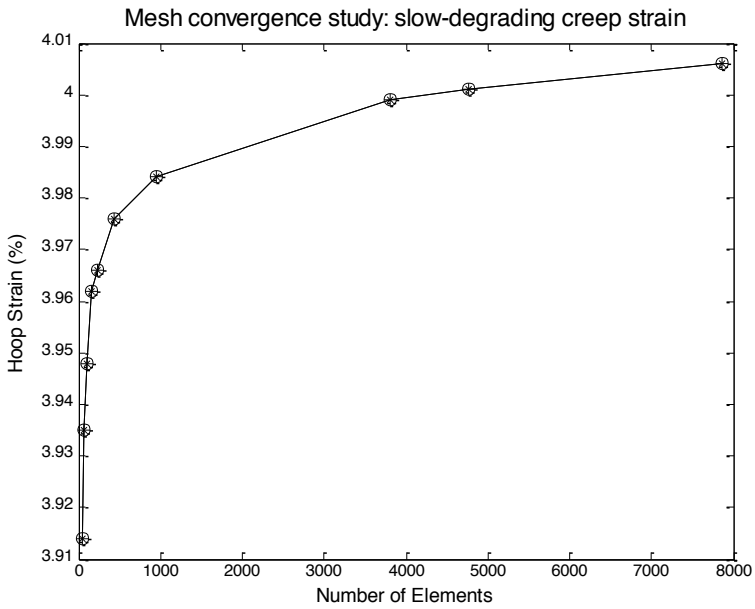

Figure 3.5: Mesh convergence plot for slow degrading PLLA.

Table 3.1: Number of elements and aspect ratio related to mesh size.

Mesh Size	Aspect Ratio	# Elements
1.00	10.00	40
0.90	9.75	44
0.80	7.82	65
0.70	7.82	70
0.60	6.53	102
0.50	5.00	160
0.40	4.36	225
0.30	3.03	429
0.20	2.07	950
0.10	1.04	3800
0.09	1.14	4773
0.08	1.27	6000
0.07	1.46	7865

Figure 3.6 depicts the meshed cylindrical annulus used for the studies presented in Chapter IV. As a result of the mesh convergence study, it was determined that the element size that corresponds to around 4000 total elements in the uniformly meshed model produces converged solutions. Because the results for the hoop strain are uniform throughout the length of the model at each radial position, a mesh gradient was applied so that the results are to be obtained and presented at the distal end of the model from the applied boundary condition on the rear face. By using the converging mesh, the computational time was greatly reduced as the total number of elements in the model was reduced to 558. For a comparison of the number of elements in each study, Table 3.1 depicts each mesh size with corresponding aspect ratio and total number of elements in the model.

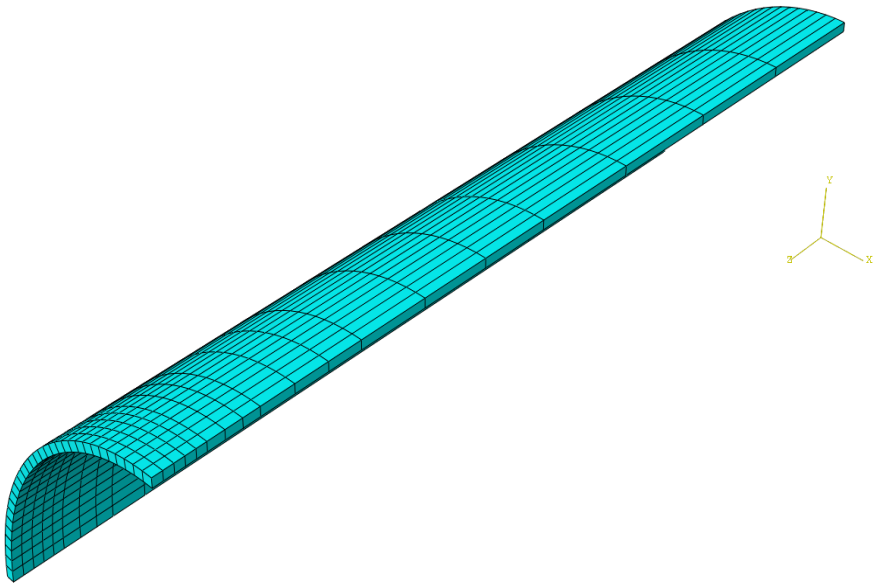

Figure 3.6: Mesh for stent model, converging to element size with aspect ratio 1.27.

For the model presented, there is only one element through the thickness of the material. A comparative study for the number of elements through the thickness that is required for converged solutions is shown in Figures 3.7 – 3.8, supporting that the results obtained at the inner and outer surfaces with 1 element thickness is roughly the same as 3 elements through the thickness of the material. For this study, PLLA material properties were utilized and a slow-degrading model was implemented. As seen in Figure 3.7, the degradation at the inner and outer surfaces for each meshed thickness is approximately the same. Figure 3.8 depicts the stress-strain curve at the inner and outer surfaces for each meshed thickness, further illustrating how various numbers of elements through the thickness result in the same values for the variables at hand.

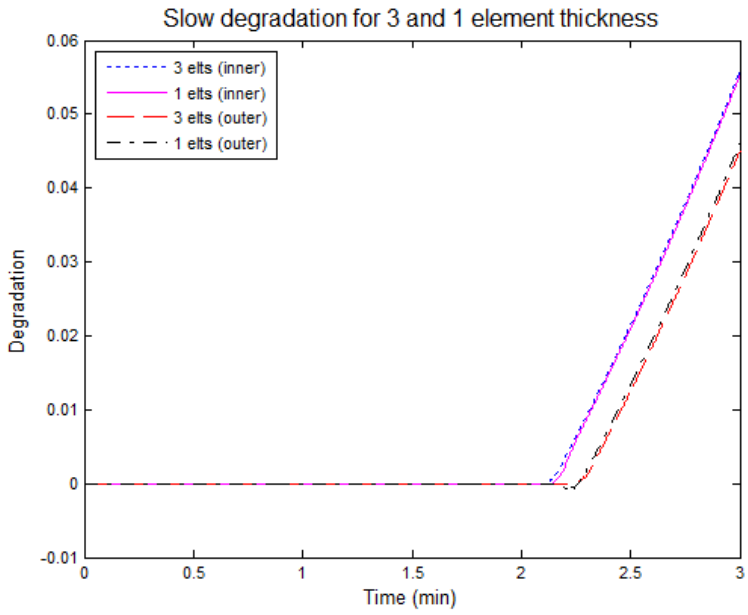

Figure 3.7: Degradation at the inner and outer surfaces for the meshed model seen in Figure 3.4, compared with three elements through the thickness.

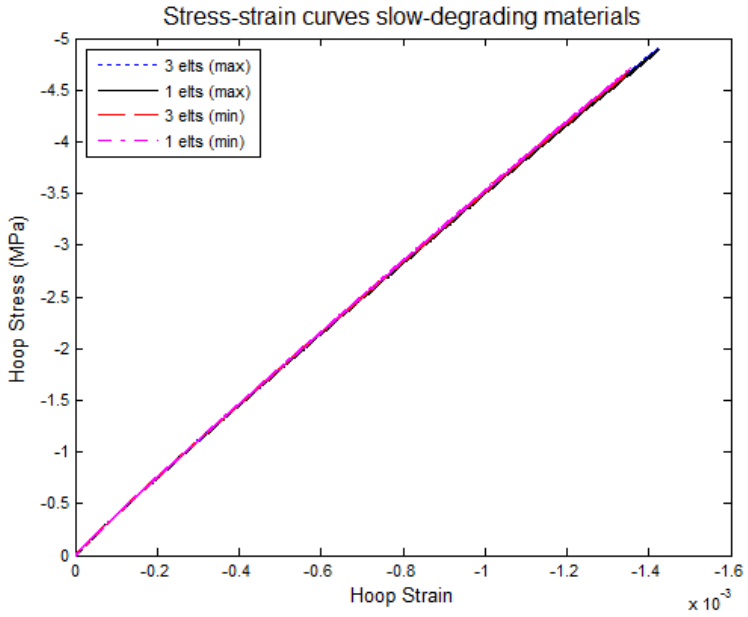

Figure 3.8: Stress-strain curves for slow-degrading PLLA at the inner and outer surfaces for models with 3 element thickness compared with model with 1 element thickness.

CHAPTER IV

SIMULATION RESULTS

4.1 Ramped Loading Study

Initial simulation was done under ramp loadings. Under this loading condition, each pressure exerted on the cylindrical annulus is ramped linearly over the assigned time of study until the magnitude of the applied pressure is reached. This analysis was conducted over a total time of 10 minutes (600 seconds) with a time increment of 0.1 seconds. Four models are studied, as each material model is subjected to slow and fast degradation. Models 1 and 2 have the material properties of PLLA that are listed in Table 2.1. For Model 1, the constant A in the degradation function in Eq. (2.24) has a value of 0.5. This model represents slow degradation of a stent comprised of PLLA. For Model 2, the constant in the degradation function has a value of 5.0. This model represents fast degradation. Models 3 and 4 have the same degradation functions as Models 1 and 2, respectively, however each model has the material properties of POM that are listed in Table 2.2. The hoop stresses and strains are calculated at the inner and outer surfaces of the stent model to determine where the maximum and minimum values occur. In addition, the degradation function is calculated at each increment at both surfaces to determine the difference in the rate of degradation and how the rates affect the stresses and strains at each location. It is noted, as mentioned in the determination of the thresholds in Chapter III, the values for the critical strains were reduced by an order of magnitude, so not to model the cylindrical annuli using the maximum capacity of the

materials. This results in the critical strains for PLLA and POM to be 0.247% and 0.230%, respectively.

Figures 4.1 – 4.3 depict the degradation for each material model under ramped loading conditions. Figure 4.1 shows the rate of degradation at the inner and outer surfaces for a model with PLLA material properties with both slow and fast degradation functions. For PLLA, degradation begins to occur after approximately 6.5 minutes of loading. For slow degrading PLLA, the degradation is linear and after 10 minutes of analysis, the degradation function at the current time and inner surface has a value of 0.288. This represents the stiffness of the material reducing to 76.96% of its original value. At the outer surface, the stiffness is reduced to 79.52% of its original value, as the degradation function at the current time has a value of 0.256. Fast degrading PLLA shows a much greater increase in degradation, which is expected due to the fast degradation considered. At 10 minutes of analysis, the degradation function has a value of 0.983 and 0.972 at the inner and outer surfaces, respectively. This relates to the stiffness reducing to 21.36% and 22.24% at the inner and outer surfaces. It is noted that as degradation occurs, the material becomes softer, thus enhancing the magnitude of the strain, which further accelerates the degradation. Figure 4.2 depicts the degradation for slow and fast degrading POM at the inner and outer surfaces. Like the previous material model, there is a linear increase in degradation at the inner and outer surfaces for a slow degrading POM, with a much faster increase in degradation in the fast degradation case. For POM, the onset of degradation does not occur until roughly 7 minutes of analysis. For slow degradation, the stiffness at the inner and outer surfaces reduce to 83.28% and

85.92%, respectively, as the degradation function has values of 0.209 and 0.176. For fast degradation, the stiffness at the inner and outer surfaces reduces to 26.08% and 29.36%, as the values of the degradation function are 0.924 and 0.883. Figure 4.3 depicts the comparison of the maximum degradation of each material model at the inner surface of each model. This shows the lag in onset of degradation between the two material models, where a stent with PLLA material properties shows to degrade at a faster rate than a stent with POM material properties over the current time of study. Though the threshold corresponding to the tensile strength of the materials is less for POM than PLLA, this was expected as PLLA experiences faster stress relaxation compared to the relaxation of POM, as indicated by the time-dependent material parameters in Tables 2.1 and 2.2.

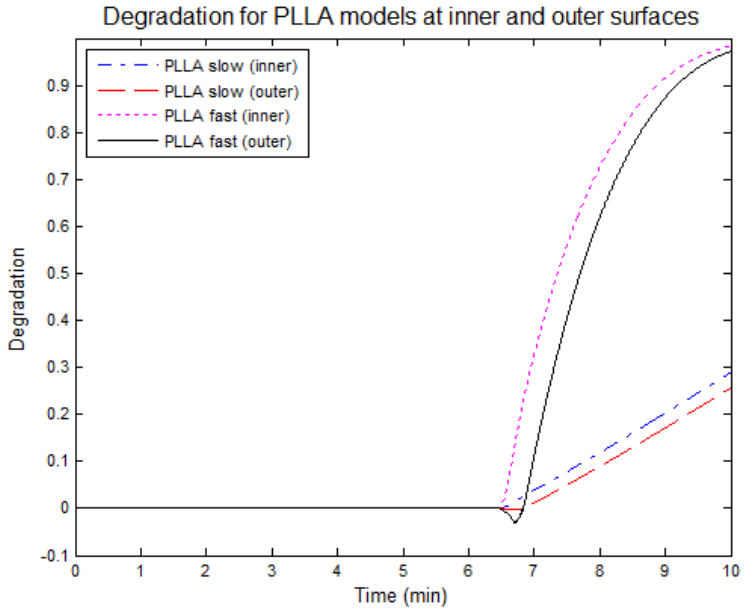

Figure 4.1: Degradation at inner and outer surfaces for PLLA material properties at slow and fast degradation.

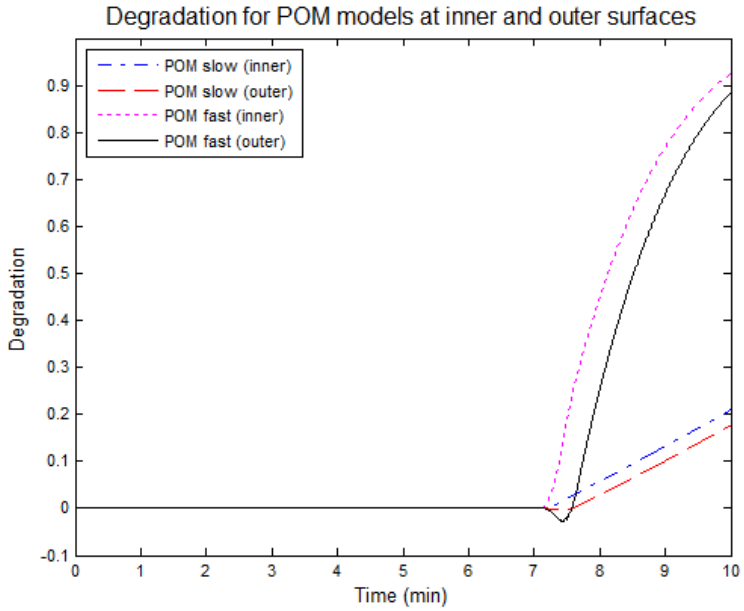

Figure 4.2: Degradation at inner and outer surfaces for POM material properties at slow and fast degradation.

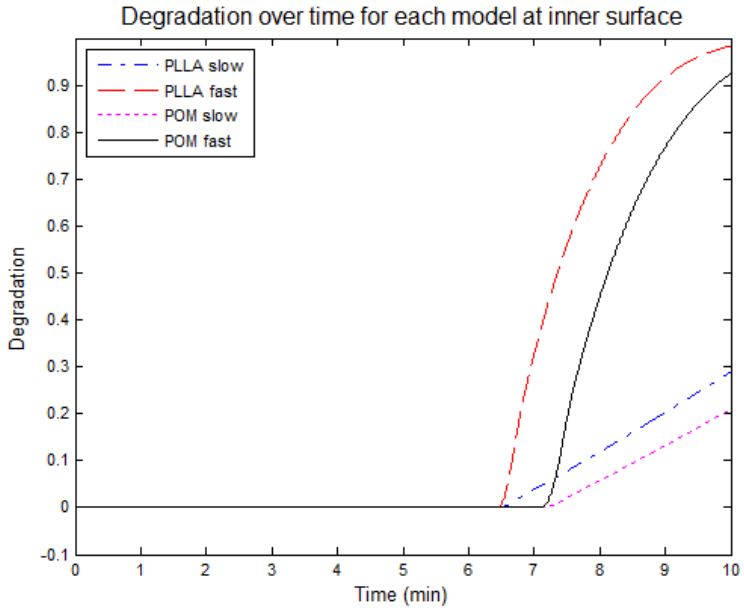

Figure 4.3: Comparison of degradation rates at the maximum value (inner surface) for both material models.

Figure 4.4 depicts the maximum hoop stresses and how they vary over time. Evidence shows that the hoop stresses that accrue in the cylindrical annulus for each model over time vary slightly, as the curves are shown nearly on top of each other. This was expected as the prescribed loading condition was stress. Figure 4.5 depicts the hoop strains for each model as a result of the prescribed ramped stresses. It is observed that the rate of strain for PLLA is faster than POM, as predicted due to the time-dependent material properties and the degradation observed previously. As well, Figure 4.5 supports the statement that as the material degrades more, the strains in turn increase, resulting in a much greater strain rate for the fast degrading models, as observed.

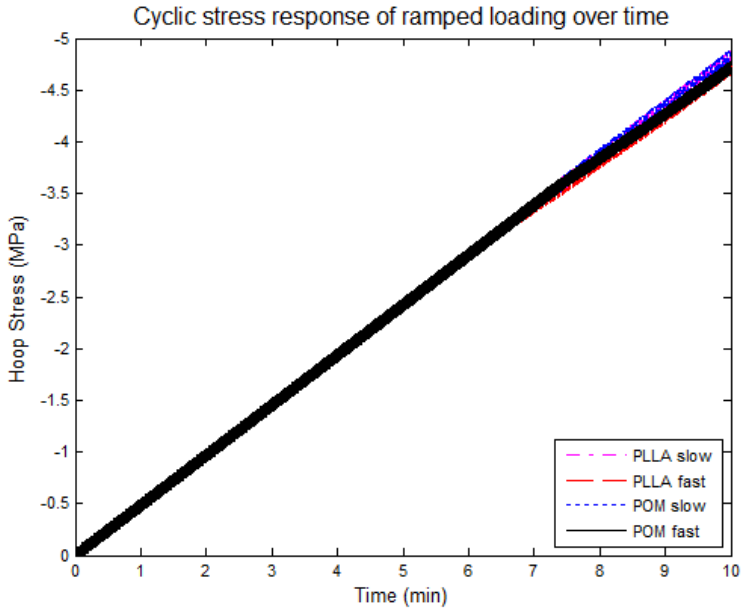

Figure 4.4: Hoop stress at maximum value (inner surface) for each material model.

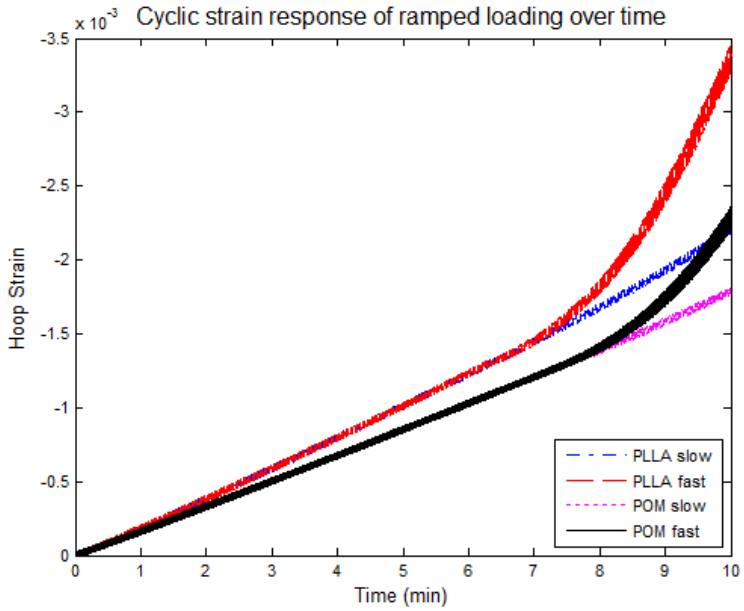

Figure 4.5: Hoop strains at the inner surface for each material model.

Figure 4.6 depicts a comparative study for the stress-strain curves for each model. Each slow degrading model has a relatively linear stress-strain curve, with POM having a higher slope than PLLA. This was expected as the time-dependent material properties in Tables 2.1 and 2.2 indicate that POM is a much more stiff material than PLLA. It is easier to see where the onset of degradation occurs in the fast degrading models, with PLLA beginning to degrade earlier on than POM. Due to the cyclic analysis being conducted over 10 minutes and the applied loads resulting in small amplitudes of stress and strain, Figure 4.6 appears to depict the stress-strain curve for a constant load. To verify the loading is indeed cyclic and to show the mechanical energy lost due to such loading, a close-up view of the stress-strain curves for cyclically loaded fast-degrading PLLA and POM is presented in Figure 4.7, in which the hysteresis observed in a loading and unloading cycle for viscoelastic materials can be seen over a

time period of 5 cycles. It is noted that POM dissipates more mechanical energy during a loading and unloading cycle than PLLA for a fast degrading material. This was predicted by comparing the time-dependent data presented in Tables 2.1 and 2.2. Figure 4.8 is presented to verify that the frequency of the loading of 1 Hz, or 1 beat per second, is maintained through the study. Here, a close-up view of the hoop stress over a period of 20 seconds is shown, in which 20 periods can be observed.

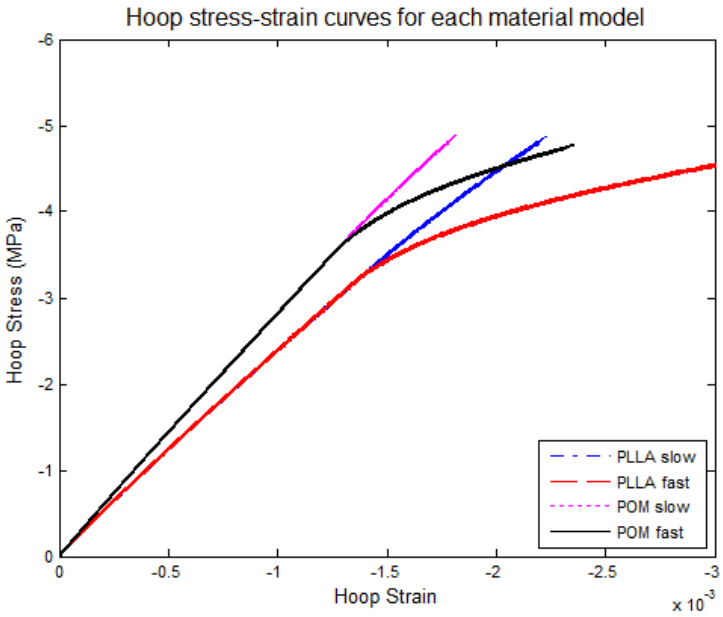

Figure 4.6: Hoop stress-strain curve for each material model.

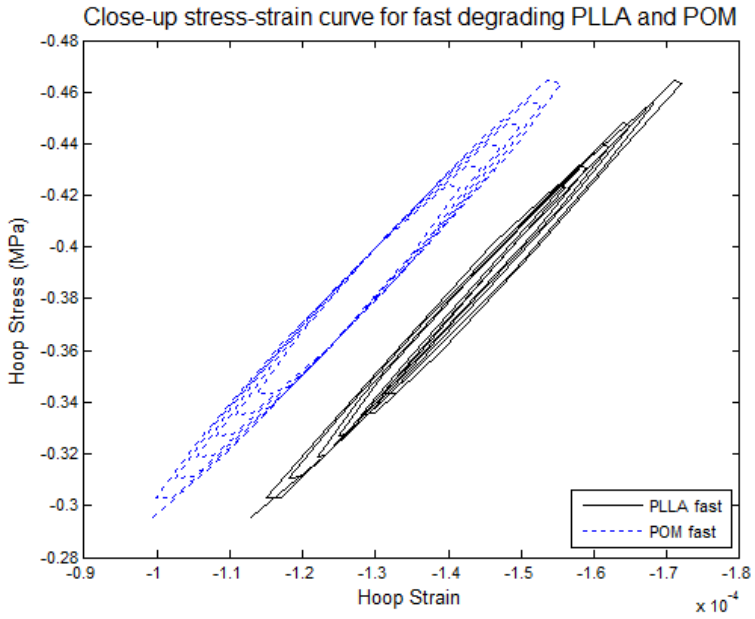

Figure 4.7: Close-up view of stress-strain curves for fast degrading PLLA and POM, showing the hysteresis that is observed for loading and unloading of viscoelastic materials.

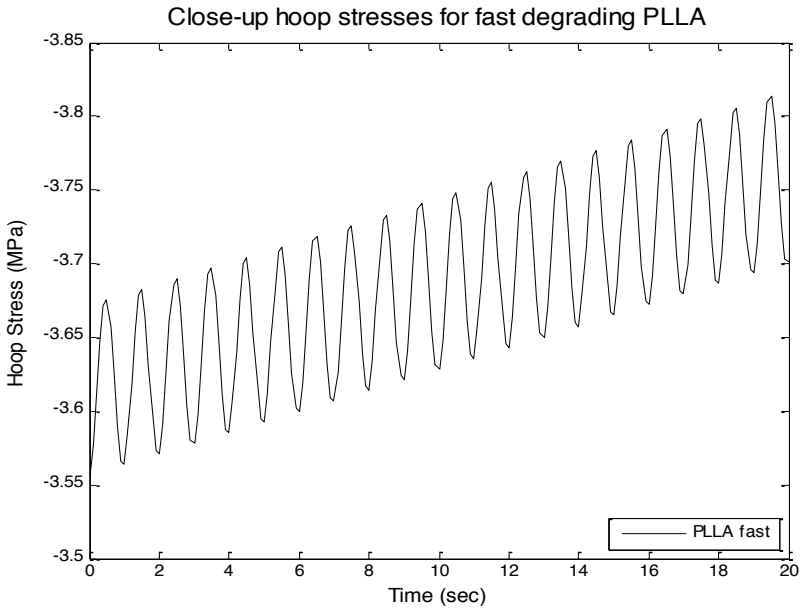

Figure 4.8: Hoop stress for fast degrading PLLA over a period of 20 seconds.

4.2 Creep-cyclic Loading Study

A next study was conducted to determine the creep deformation of each model over time. In this analysis, each load is maintained at its assigned value throughout the study. This analysis allows for a better understanding of how the different time-dependent properties for each material affect the deformation under the same loading conditions. The crushing pressure of the arterial wall is maintained constant at 2 atm, while the simulated blood pressure oscillates between 120 mmHg and 80 mmHg at a frequency of 1 Hz throughout the study. Once again, the thresholds corresponding to when degradation will onset were assigned to be 0.247% and 0.230% strain for PLLA and POM, respectively.

Figures 4.9 and 4.10 depict the degradation over time for each material model and each rate of degradation at the inner and outer surfaces. As was expected, the larger values of degradation occur at the inner surface for each model. Figure 4.9 shows the difference in degradation at the inner and outer surfaces for slow and fast degrading PLLA. For slow degrading PLLA, the inner surface degrades to a value of 0.700 while the outer surface yields a value of 0.679. This corresponds to a reduction in material properties at the inner and outer surfaces of a slow degrading PLLA stent to 44.00% and 45.68% of their initial value, respectively. For the fast degradation model, degradation to 20% of the original value of the material properties is observed after roughly 4.0 minutes of analysis at the inner and outer surfaces. Figure 4.10 depicts the degradation of slow and fast degrading POM. At the inner and outer surfaces of the slow degrading model, the degradation function has a value of 0.626 and 0.605, respectively, reducing the

material properties to 49.92% and 51.60%. As was the case for fast degrading PLLA, fast degrading POM degrades to 20%, but after roughly 4.5 minutes of analysis, as opposed to 4.0 minutes for PLLA. Figure 4.11 presents a comparative study of the rate of degradation at the inner surface for each model. As is observed, PLLA degrades faster than POM. In addition, it is noticed that the difference in the rate of degradation between the two material models is greater in the slow degrading studies. This verifies that the rate of loading affects how the material deforms, as well as the magnitude of the load. By increasing the value of the constant *A* in the degradation function, simulating an increase in the rate of loading, the materials begin to move towards the same rate of degradation. As a result, the deformation exhibited by each material model is more similar.

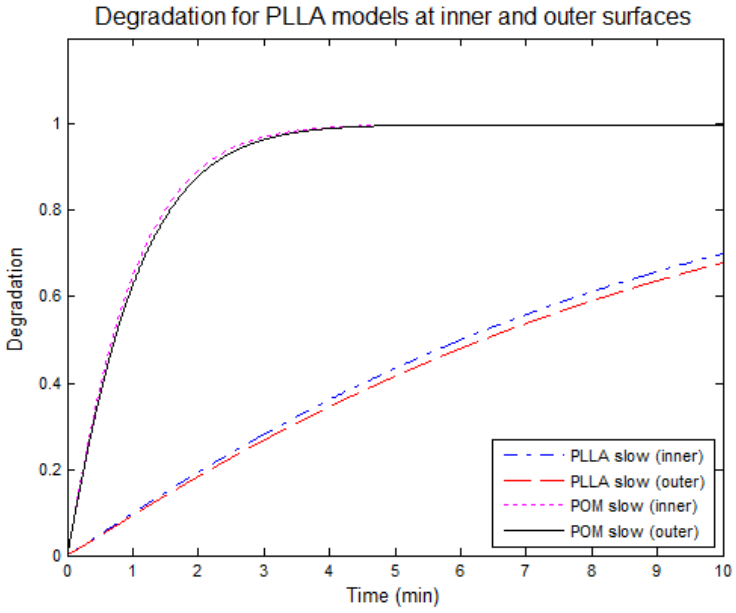

Figure 4.9: Degradation rates for PLLA material properties at the inner and outer surfaces due to cyclic loading.

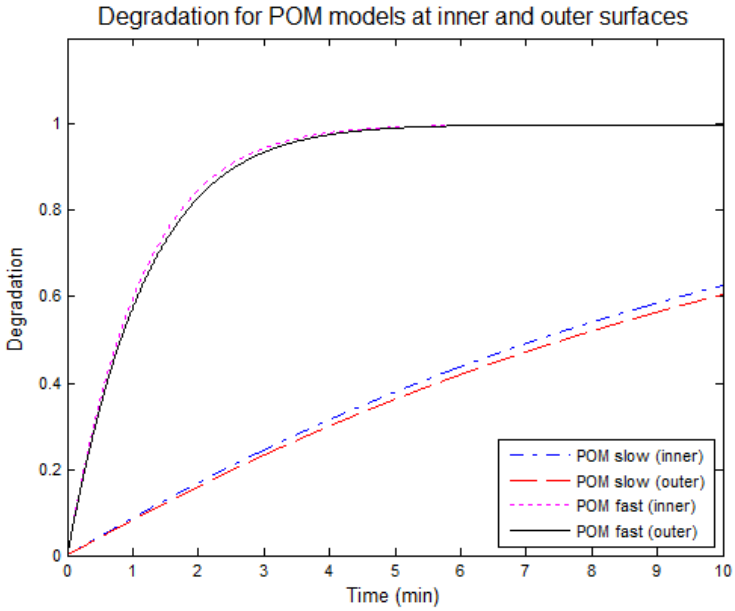

Figure 4.10: Degradation rates for POM material properties at the inner and outer surfaces due to cyclic loading.

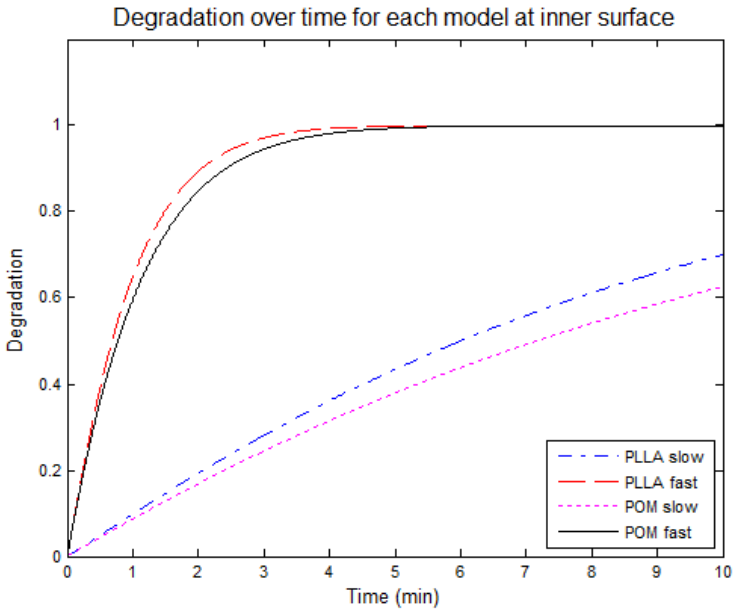

Figure 4.11: Comparison of the degradation rates of each material property at the maximum value.

Figure 4.12 depicts the creep strain over time for each model at the inner surface. As expected, for faster degradation the strains begin to oscillate with a greater amplitude compared to that of the slow degrading models. As was the case with the strain response observed in the ramped loading cases, Figure 4.12 provides support that as the materials are strained more, more degradation occurs leading to yet more of an increase in strain as the cycle repeats itself. As well, the strains for the faster degradation study are still increasing over time at the end of the analysis, whereas for the slower degradation models the strains appear to be approaching a constant amplitude. This is most certainly due to the material properties for the fast degrading models reducing to 20% of their original value early on, thus continuing to strain much more over time versus the slow degrading models.

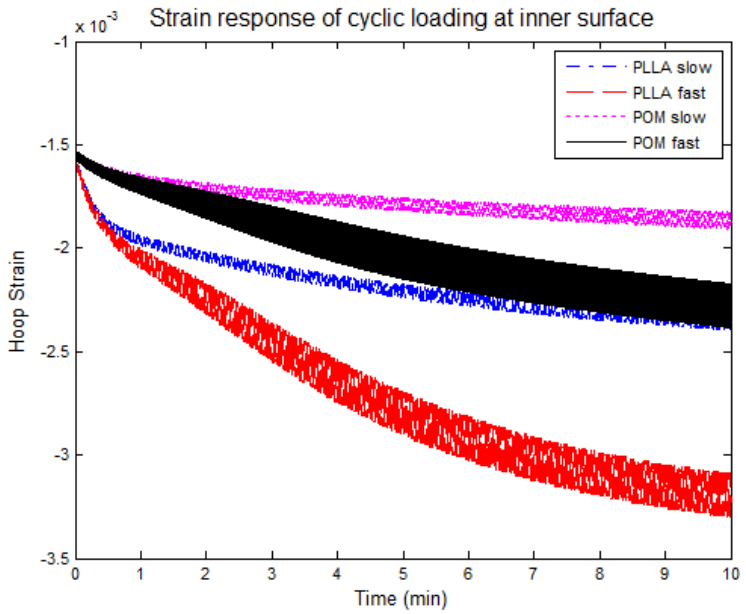

Figure 4.12: Hoop strain response due to cyclic loading at the inner surface.

4.3 Realistic Stent Geometries Study

After different loading conditions were studied for each material with a cylindrical annulus, final analyses were conducted using realistic geometries that are used for cardiovascular stents in the current market. This study was conducted to gain a better understanding of how a stent might deform given the constitutive relations and material properties defined in Chapter II. As well, the location of stress concentrations that accrue due to the geometry is accounted for which can accelerate the degradation at these locations. Figure 4.13 depicts the geometry for a standard wire-meshed stent that was developed in SolidWorks, CAD software that is available in computing laboratories at Texas A&M University's Department of Mechanical Engineering. The inner diameter of the stent is 2.4 mm, with a thickness of 100 μm. The width of the cross-hatched pattern links are equal to the thickness and the overall length of the stent is approximately 20 mm. Moore et al. [9] stated that because of the repeating nature of the rings in stent designs and the fact that any effects from the edges of the stent dissipate within the first segment, the mechanical environment in the middle section of a given stent model is equivalent to the mechanical environment of any two inner rings of a full length stent. Because of this, only a portion of the stent along its length is needed for analysis, which is depicted in Figure 4.13 as well. In addition, two models with this geometry were analyzed. First, the model was analyzed without inclusion of fillets resulting in points of singularities at the sharp angles. Next, fillets with radii of 75 μm were applied to each angle within the mesh, thus removing singularity points and reducing stress concentrations.

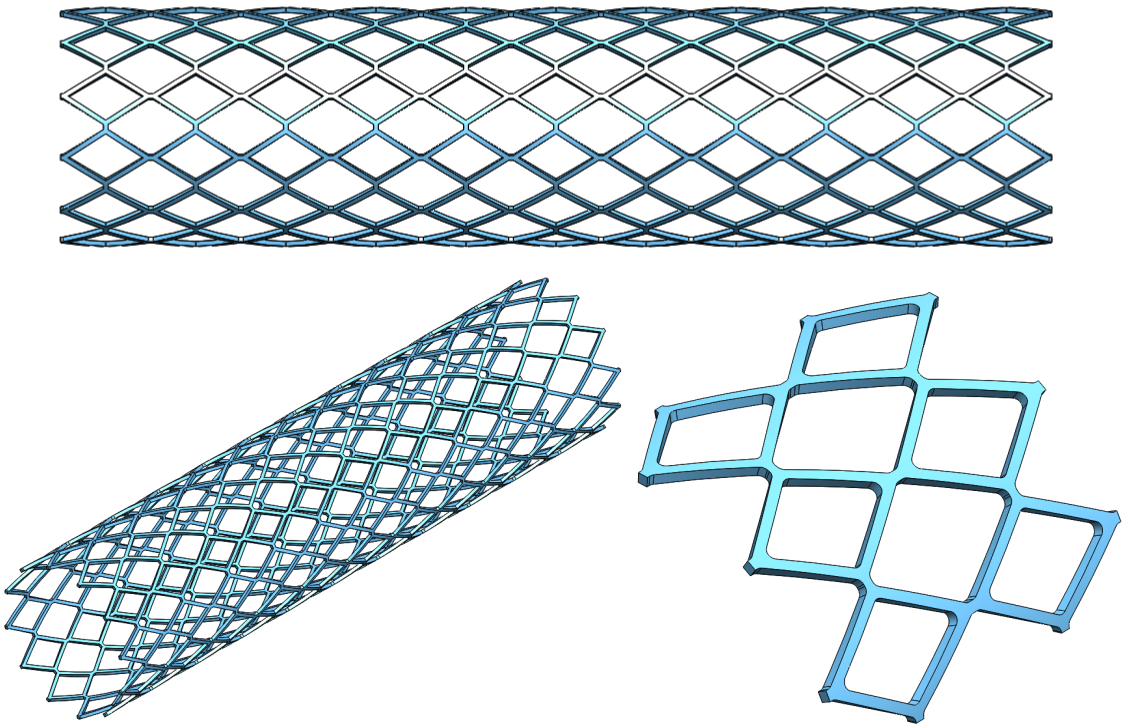

Figure 4.13: Top: Side-view of a cross-hatched pattern stent developed in SolidWorks, depicting the repeating nature of the meshed rings. Bottom-left: Three-dimensional view of the stent. Bottom-right: Close-up view of the stent portion analyzed in ABAQUS (two repeating rings).

A mesh convergence test was conducted over 20 seconds utilizing a time increment of 0.1 seconds. PLLA material properties were chosen along with a slow degrading constitutive model. The same pressures applied to the cylindrical annulus during the creep-cyclic study were applied to the outer and inner surfaces of the cross-hatched geometry (i.e. simulated constant arterial pressure and cyclic blood pressure, respectively). The radial displacement at the distal end of the applied boundary conditions and centered in the mesh junction was plotted with an increase in number of total elements. As can be seen in Figure 4.14, the radial displacement in the model without inclusion of fillets begins to depict convergence from approximately 15,000

total elements to 20,000 total elements. Because of the computational cost of analyzing models with large numbers of elements, the lesser total was chosen, corresponding to 14,996 total elements. It was determined that for the purpose of presenting a qualitative study with non-uniform distributions of stresses and strains, this mesh would suffice. Figure 4.15 depicts the mesh convergence for the same design, with inclusion of fillets at the angles as previously mentioned. Here, the convergence is shown to be much more smooth, though the total number of elements at convergence is slightly higher. For this model, the mesh size corresponding to 17,764 total elements was chosen.

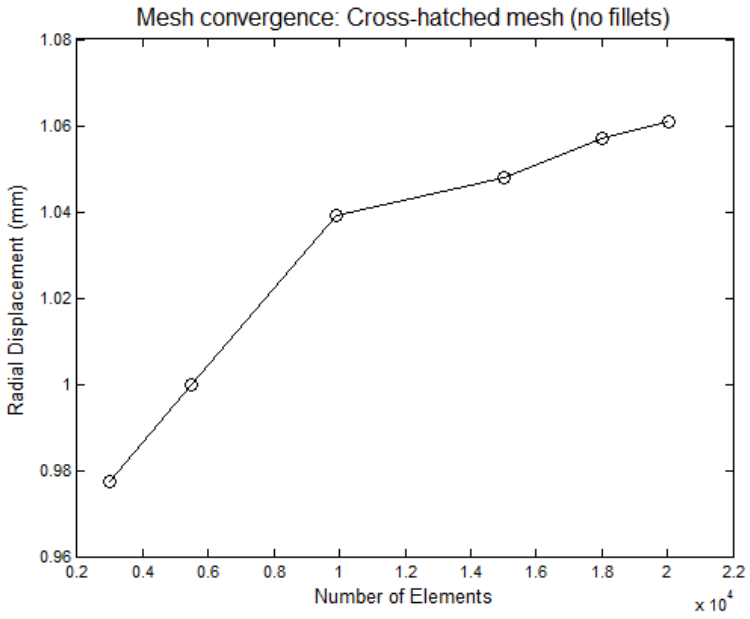

Figure 4.14: Mesh convergence study for a cross-hatched stent geometry without inclusion of fillets.

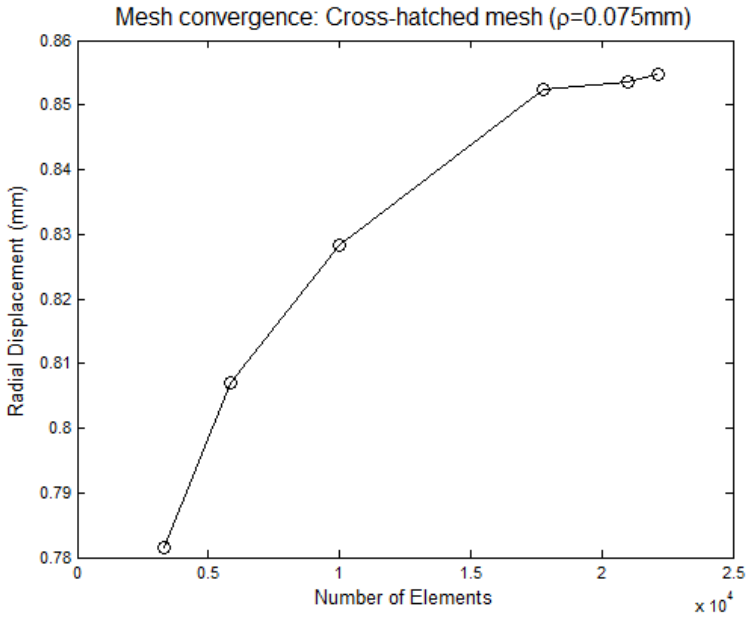

Figure 4.15: Mesh convergence study for a cross-hatched stent geometry with inclusion of fillets with radius of 75 micrometers at each sharp angle.

A creep-cyclic study was conducted over a period of 1 minute on each model using slow degrading PLLA material properties. The pressures applied to the external and internal surfaces were the same as applied in the creep-cyclic study of a cylindrical annulus (same as for the mesh convergence study). Figure 4.16 depicts a close-up view of the hoop stresses that accrue at the junctions in each model. It is noted that the stresses are distributed more evenly across the junction in the second model, resulting in a reduced magnitude in stress concentrations. This was expected due to the inclusion of fillets in the second model and the fact that stress concentrations are at a maximum where the radius of curvature is at a minimum.

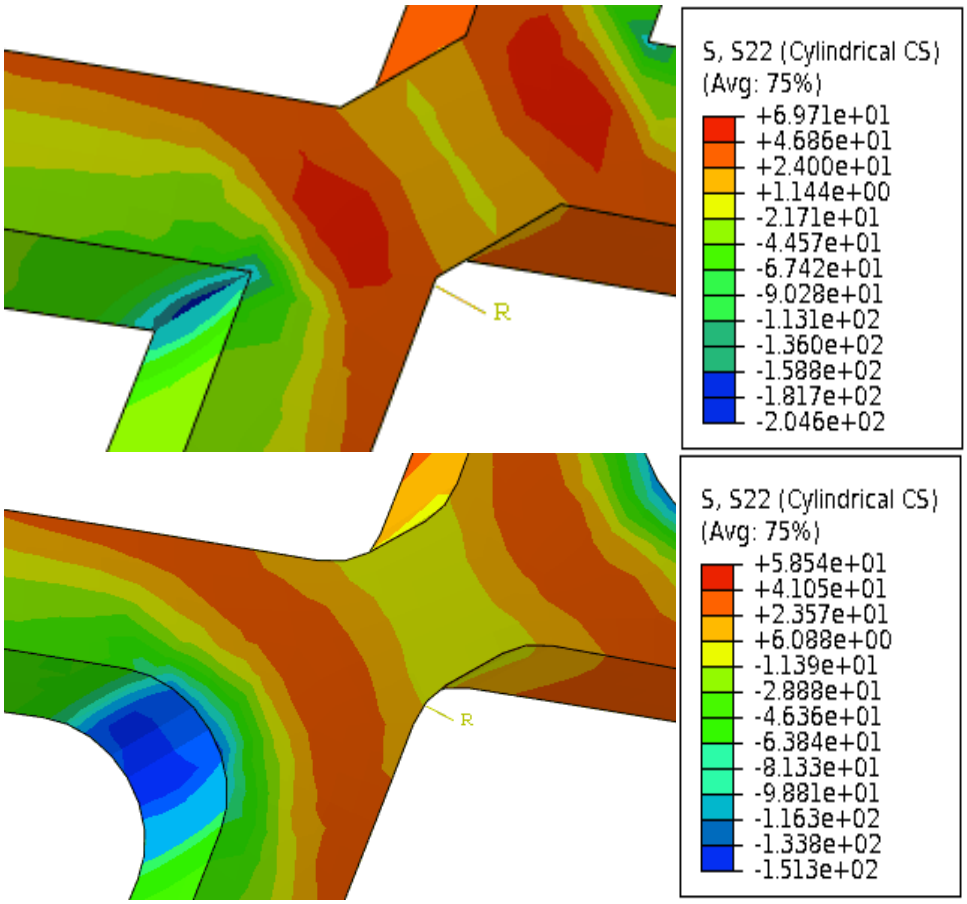

Figure 4.16: Top-left: Close-up view of the site of maximum stress concentrations without inclusion of fillets. Top-right: Magnitude of hoop stresses distributed throughout the stent model (units in MPa). Bottom-left: Close-up view of the site of maximum stress concentrations with inclusion of fillets. Bottom-right: Magnitude of hoop stresses distributed throughout the stent model (units in MPa).

Before going further, it is worth noting that in the previous sections, solutions obtained and presented were taken at the nodal values. Due to the fine mesh size utilized for the simplified geometry in the cylindrical annulus, the results observed at the integration points and the corresponding nodal values varied only slightly, as seen in Figure 4.17, where the maximum hoop stresses are compared. For the geometries presented in this section, this is not the case. Figure 4.18 presents a comparison of the maximum stress concentrations taken at the nodal value and the value obtained at the

integration point for the model without inclusion of fillets. As depicted, there is a difference in hoop stress at the location of maximum stress concentration of approximately 40 MPa. This difference in value is due to the mesh size utilized for the cross-hatched mesh model. The mesh size utilized to conserve computational cost for this analysis resulted in large differences in the nodal values and values obtained at the integration points. Thus, further results shown are depicted at the integration points. Improvement in quantitative results can be achieved by considering finer meshes and incorporation of a proper nonlinear constitutive model for the polymers.

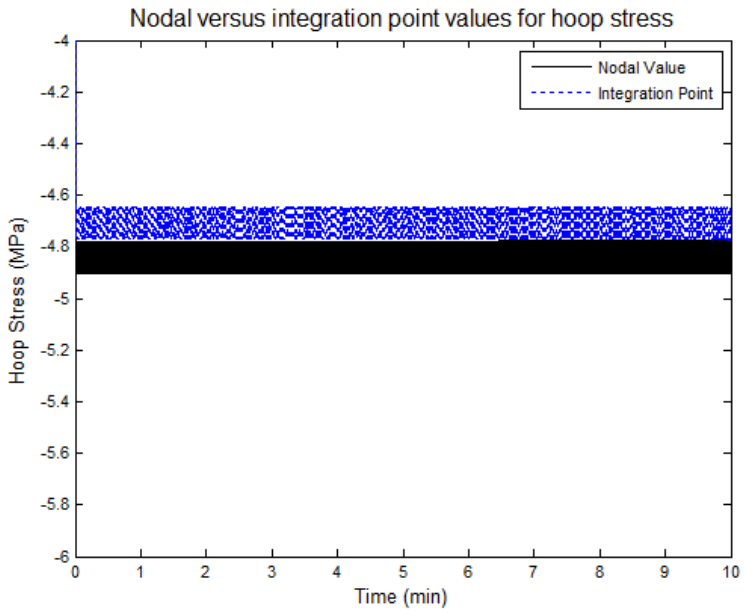

Figure 4.17: Maximum hoop stress comparison of nodal value and value taken at the integration point in the cylindrical annulus model.

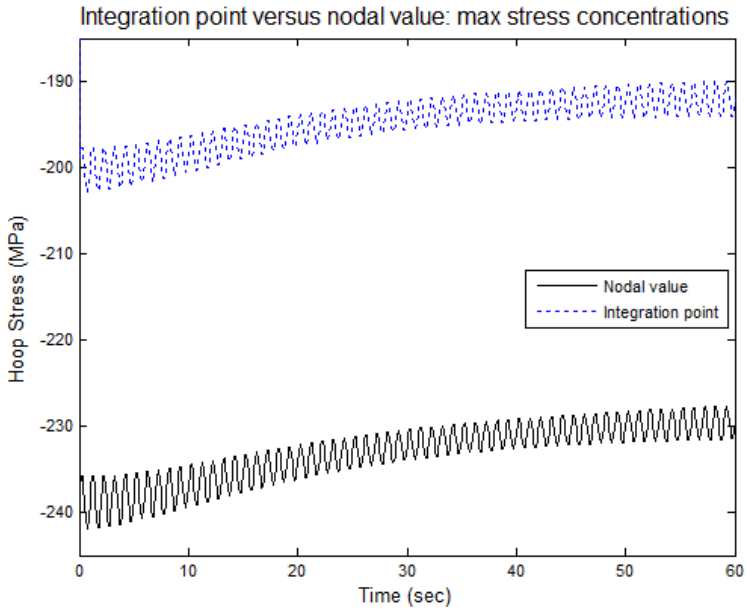

Figure 4.18: Stress concentration comparison taken at the maximum nodal value and the integration point in the cross-hatched mesh stent geometry.

Figures 4.19 and 4.20 depict the maximum hoop stresses at the mesh junctions for the model without fillets and the model with fillets, respectively. It is first noted that the stresses that develop in the material are much higher than those observed using a simplified cylindrical annulus model. This was also predicted as the geometrical properties of the material decreased by introducing the voids associated with the cross-hatched pattern, thus causing the stresses to increase. The cyclic hoop stress response shown in Figures 4.19 and 4.20 depict a material where the stresses relax over time, though the magnitude of the relaxation observed in the model without inclusion of fillets is greater. Figure 4.21 and 4.22 depict that cyclic creep strain response at the same location for each model. In each figure, creep deformation is observed along with stress relaxation, with the magnitude being greater for the model without fillets, once again.

The cause for the increase of magnitude in the hoop stresses and strains for the model without fillets is due to the sharp angle resulting in a singularity point. The combination of stress relaxation and creep that is observed at this junction could be a result of how the material degrades and deforms at the site of stress concentrations. At the start of loading the angles are smaller in the pattern, but as the material degrades, the radius of curvature might increase, causing the stresses to relax. The strains continue to increase as the thickness of the material decreases over time with degradation.

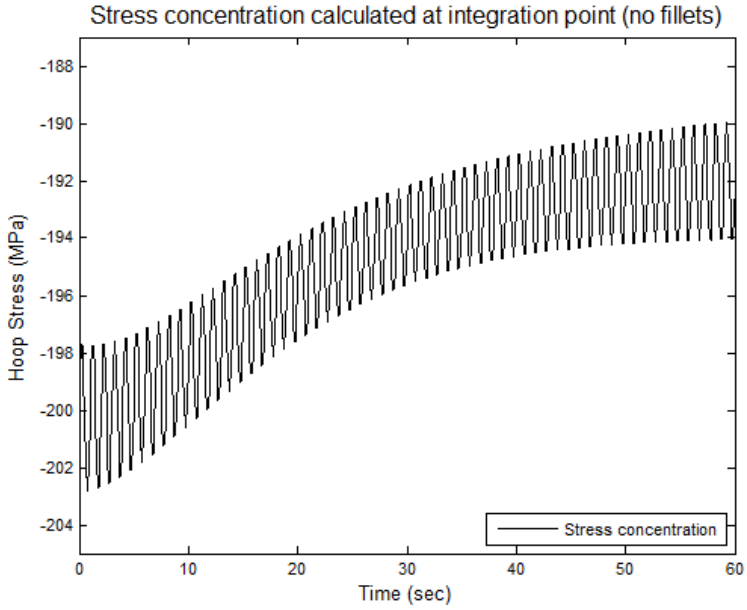

Figure 4.19: Hoop stresses over 1 minute at the site of maximum stress concentration in the cross-hatched stent geometry without fillets.

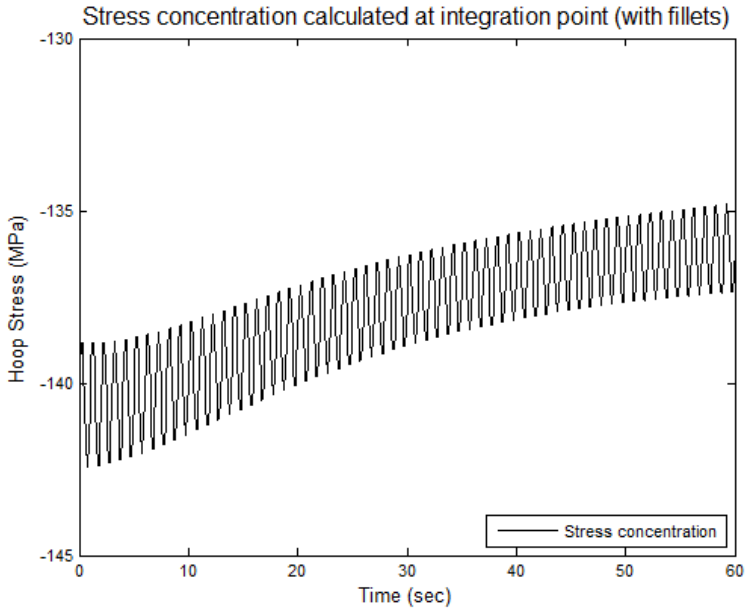

Figure 4.20: Hoop stresses over 1 minute at the site of maximum stress concentration in the cross-hatched stent geometry with inclusion of fillets with radii of 75 micrometers.

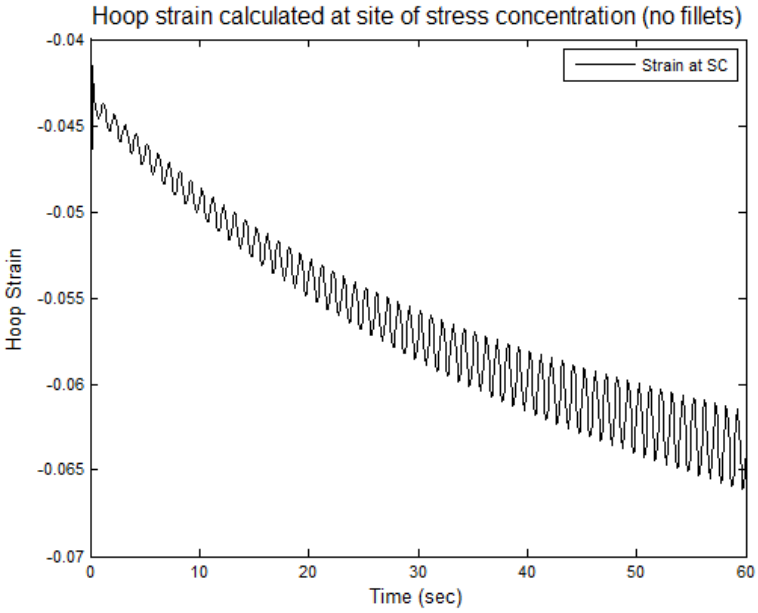

Figure 4.21: Hoop strains over 1 minute at the site of maximum stress concentration for a cross-hatched stent model without inclusion of fillets.

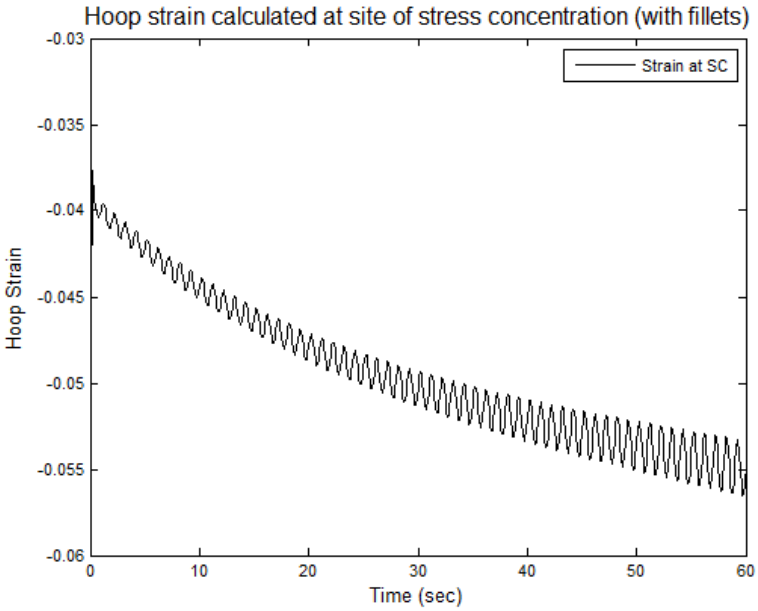

Figure 4.22: Hoop strains over 1 minute at the site of maximum stress concentration for a cross-hatched stent model with inclusion of fillets with radii of 75 micrometers.

In addition to presenting the location and magnitude of stress concentrations, how the stresses vary at points away from the stress concentrations are observed. Figures 4.23 and 4.24 present the hoop stresses at approximately 55 μm and 110 μm away from the site of maximum stress concentration in each model. Slight stress relaxation is observed at 55 μm from the maximum stresses in each case, whereas the stresses oscillate between relatively constant values at 100 μm away. Additionally, it is noted that the reduction in stresses at points away from the site of stress concentration is greater in the model without fillets. This was shown in Figure 4.16, where the stresses were distributed better at the junction in the model with fillets, resulting in a lesser magnitude in stress concentrations and a gradual decrease in magnitude as points move away from this location. This difference in stress response can be predicted by observing

the hoop strains at the same locations. As seen in Figure 4.25, the cyclic hoop strain at 55 µm for the model without fillets shows a greater creep response from 0.8% strain to just under 1.2% strain with increasing amplitudes, whereas the strains observed at 110 µm show an increase in strain from approximately 0.2% to 0.3%. In comparison, strains observed in the model with inclusion of fillets in Figure 4.26 show an increase from 1.4% to 2.1% at 55 µm away from the location of stress concentrations, whereas at 110 µm the strain remains constant at 0.1% strain. As was the case with the stresses, the strains reduce more away from the site of stress concentration in the model without fillets.

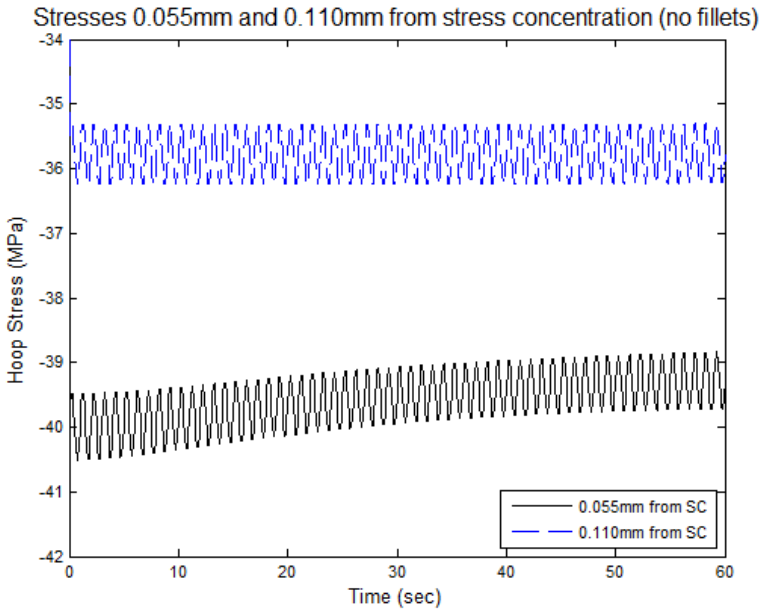

Figure 4.23: Hoop stresses at 55 micrometers and 100 micrometers away from the site of maximum stress concentration in the model without fillets.

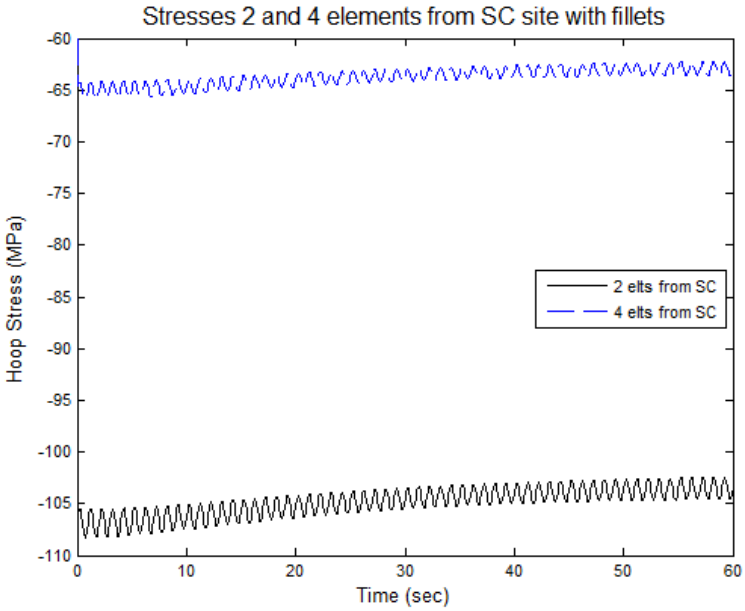

Figure 4.24: Hoop stresses at 55 micrometers and 100 micrometers away from the site of maximum stress concentration in the model with fillets.

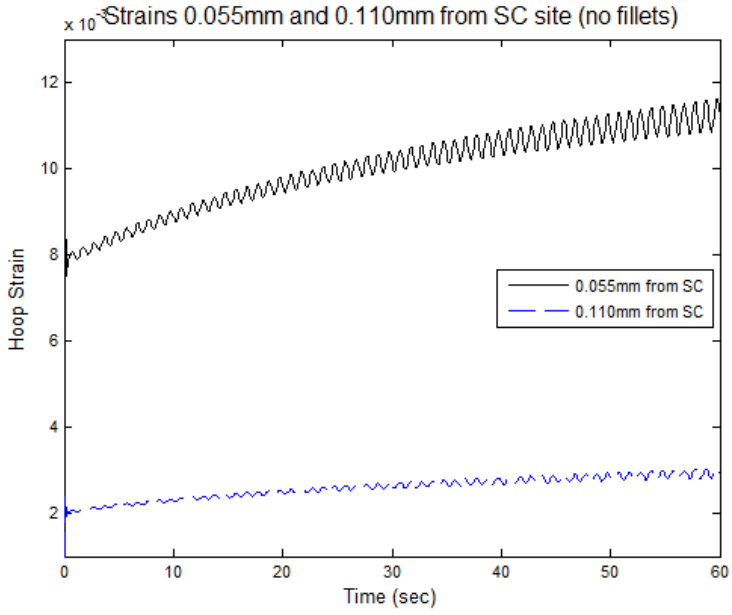

Figure 4.25: Hoop strains at 55 micrometers and 100 micrometers away from the site of maximum stress concentration in the model without fillets.

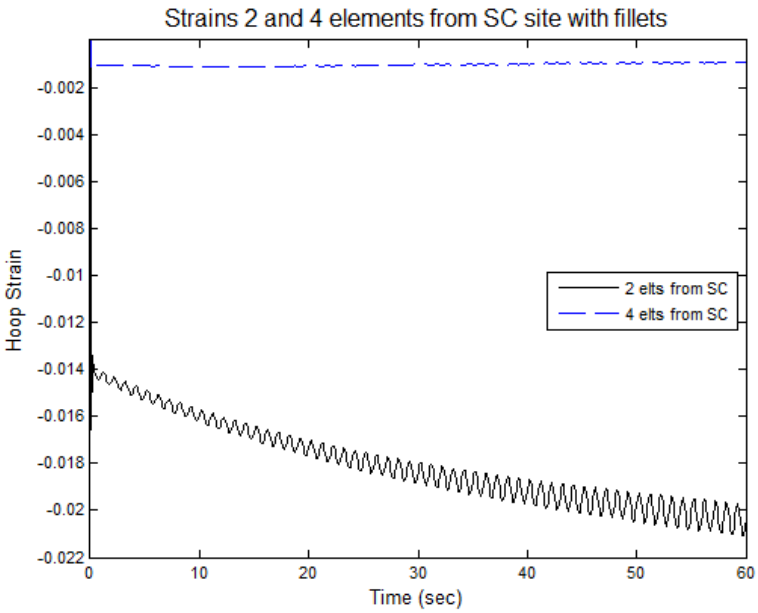

Figure 4.26: Hoop strains at 55 micrometers and 100 micrometers away from the site of maximum stress concentration in the model with fillets.

By plotting the degradation over time, as well as the maximum degradation value at points along the length of the mesh bar, an understanding of the difference in stresses and strains presented in each model can be developed. Figure 4.27 depicts the degradation at the same locations presented for the stresses and strains along the length of the bar. The scalar degradation values are plotted at the final time increment (t = 60 seconds). In the case for the model without fillets, an immediate decrease at points away from the stress concentration is depicted. For the model with fillets, there is a slight increase before a sharp decrease away from the same location. This can be explained by observing the difference in the distribution of stresses in Figure 4.16 due to the change in geometry with the introduction of fillets. The change in geometry results in the material being thinner away from the center of the fillet, where the circumferential stresses will

act to deform the model more at these locations. Thus, the strain-induced degradation will be slightly greater at this point. Figure 4.28 depicts the degradation over time for each model at the location of stress concentration and away from this location. Though the UMAT subroutine used in this analysis was that of a slow degrading material, the degradation response observed in Figures 4.28a and 4.28b resembles that of a fast degrading material as depicted in the studies with the cylindrical annulus. This is due to the change in geometry and the introduction of the voids in the model, thus causing localized stresses and strains at the junctions in the mesh at a greater magnitude than the uniform stresses and strain in the previous models, in turn ramping the rate of degradation.

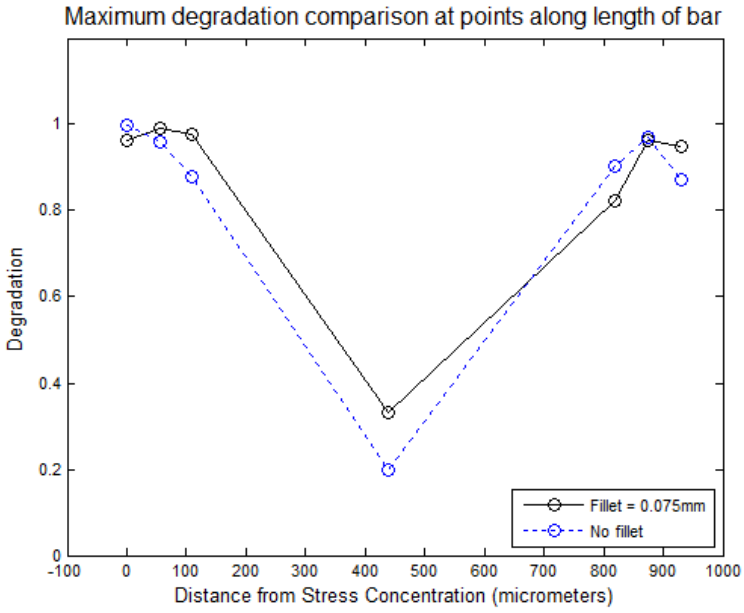

Figure 4.27: Degradation at the site of stress concentrations and how degradation varies as points move away and towards the location of positive stress concentrations at the greater angle (plotted at t = 60 seconds).

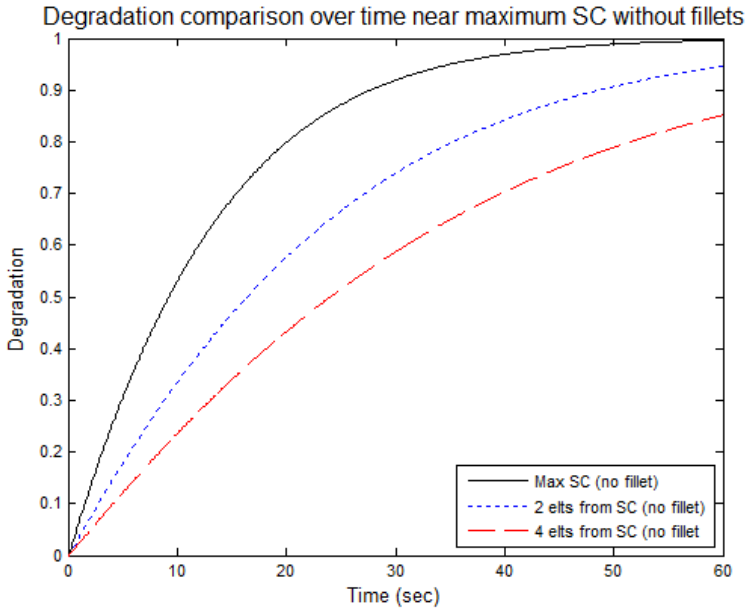

(a)

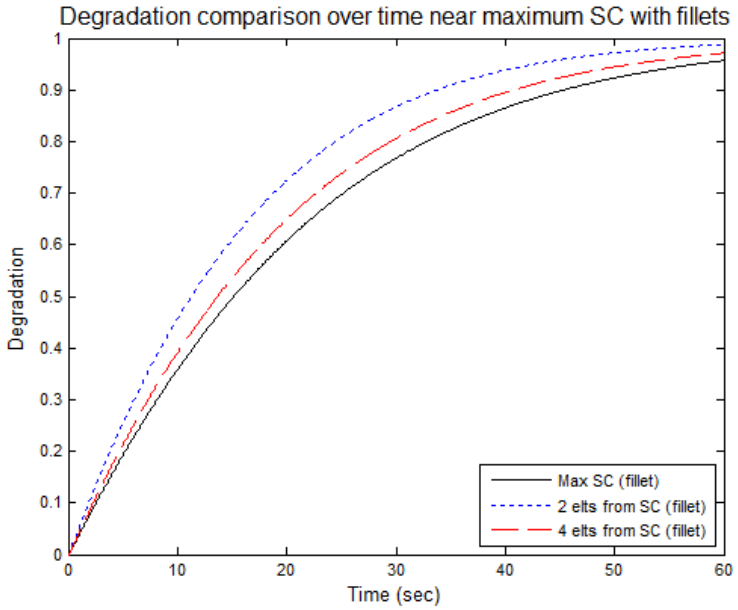

(b)

Figure 4.28: (a) Degradation over time at the site of maximum stress concentration and at points away from this location for without fillets. (b) Degradation over time at the same locations with fillets.

Figure 4.29 depicts the maximum hoop stresses at each position analyzed as the integration points move away from the location of maximum stress concentration and towards the location of positive stress concentrations (the angles at which opening mode

failure would occur) for each model. As depicted in previous plots of the stresses for each model, a sharper decrease in stress from the site of maximum stress concentration to 55 µm away is observed for the model without fillets. The hoop stress continues to decrease in relatively linear fashion until the stresses change from compression to tension (negative to positive) at roughly halfway along the length of the mesh links. Due to the geometry of the mesh, the stresses at the opposite end are in tension. This was predicted as the angles facing around the circumference of the stent will be forced to open due to the hoop stresses. The more gradual decrease in stress away from the stress concentrations is observed for the model with fillets, as mentioned previously.

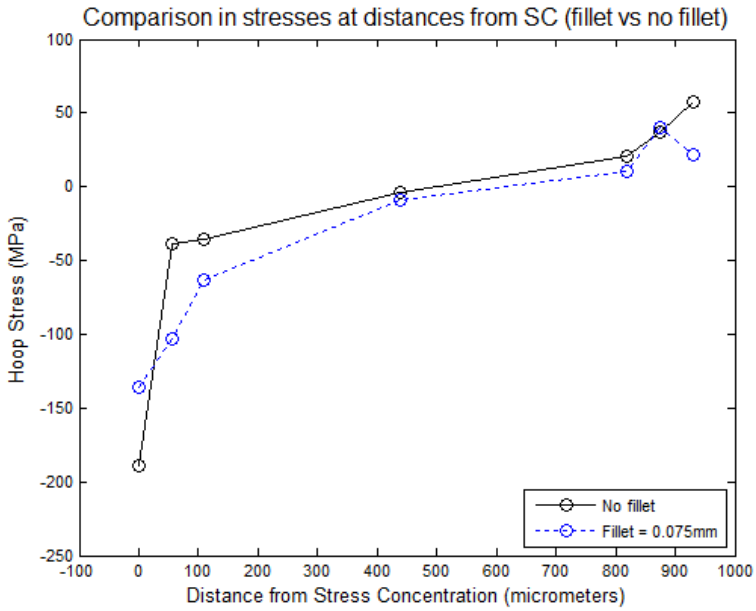

Figure 4.29: Maximum hoop stresses for each model (fillet vs no fillet) at the site of maximum stress concentration and at points away from.

In addition to the cross-hatched pattern design, another typical geometry for stents in today's market was modeled and analyzed. This design consists of curvy repeating rings connected by straight bars known as struts. Again, the inner radius is 2.4 mm with a thickness of 100 μm. The strut length is approximately 1.9 mm. The rings in the model consist of a wavy design with a radius of curvature of 0.3 mm. In addition, the struts connect at every other amplitude and are offset by one between rings. At the point of connection, fillets with a radius of 75 μm are added to reduce the stress concentrations at the junctions. Figure 4.30 depicts the design for this model.

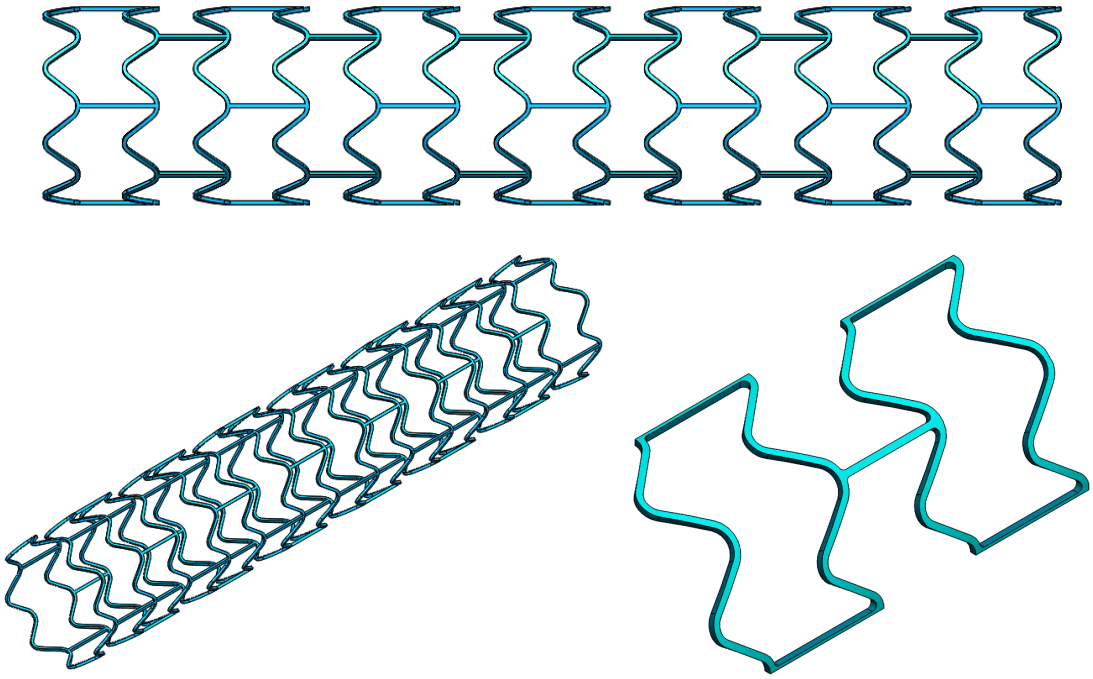

Figure 4.30: Top: Side-view of a curvy repeating ring pattern stent developed in SolidWorks, depicting the repeating nature of the meshed rings. Bottom-left: Three-dimensional view of the stent. Bottom-right: Close-up view of the stent portion analyzed in ABAQUS (two repeating rings).

A mesh convergence study was once again conducted as a new geometry was introduced for analyses. As was the case for the previous model, the study was conducted over 20 seconds at a time increment of 0.1 seconds. The same arterial pressure was applied to the outer surface and the oscillating pressure simulating blood pressure was applied to the inner surface. Figure 4.31 depicts the radial displacement at the maximum value (the amplitude without a strut connection) as the total number of elements is increased. As shown, convergence is reached with a mesh size associated with 10,797 total elements.

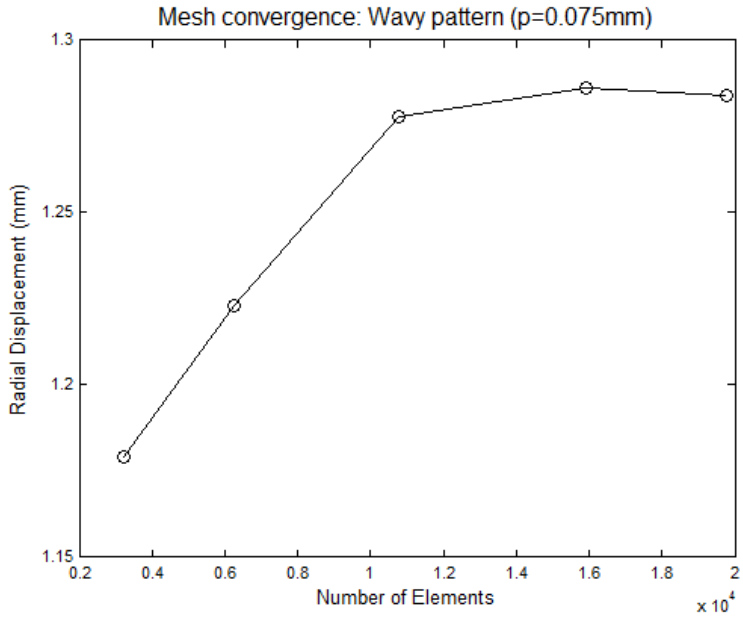

Figure 4.31: Mesh convergence study of a stent geometry consisting of repeating rings connected via straight bar struts.

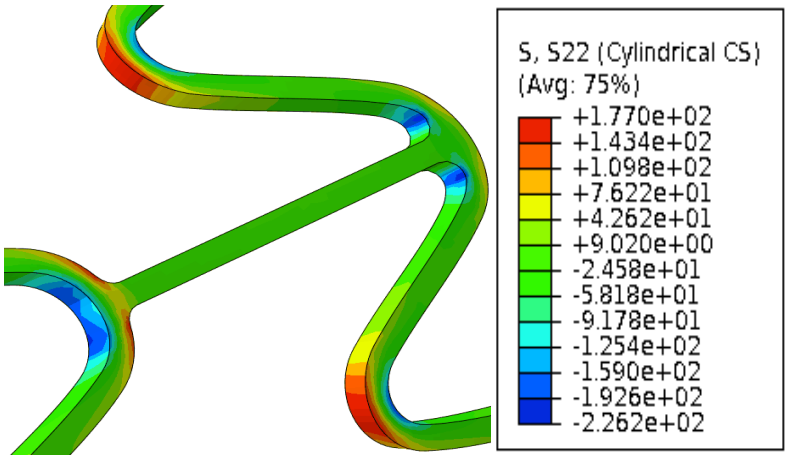

Figure 4.32: Left: Location of stress concentrations in the model at strut connections at each end. The maximum value of stress concentration as depicted on the right is on the reverse side of the amplitude depicting maximum tensile stress. Right: Magnitude of the stresses distributed throughout the model (units in MPa).

The hoop stresses and strains due to compression and tension, along with the degradation over time, are plotted at three different locations. These locations include each end at which the struts connect to the repeating rings and the maximum values of stresses and strains where there are no strut connections. The three locations at which the results are plotted are depicted in Figure 4.32, along with the maximum value of the stress concentration. Figures 4.33 and 4.34 depict the hoop stresses at each location in compression and in tension, respectively. It is noted that the magnitude of stresses that accrue in this model are higher than that in the previous model. This is due to the geometry of the model having greater curvatures than shown previously. In addition, it is seen how the various radii in the model affect the stresses that accrue at the respective locations. As expected, Figure 4.33 shows the strut connection corresponding to the smaller radius of curvature having an increase in stress concentration due to compression over the opposite end, whereas the location without a strut junction has the greater of all three. Figure 4.34 depicts the stresses due to tension at each location. The greatest value

in tension is located where the strut connects to the convex curve where the minimum is located at the concave curve. The value of hoop stress at the location without a strut connection is between the two.

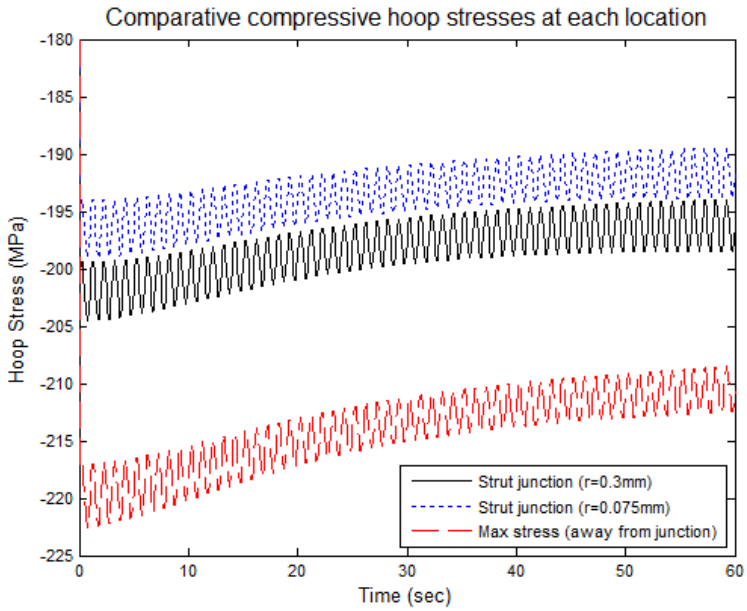

Figure 4.33: Hoop stresses due to compression at each of the three locations (i.e. each strut connection at the junctions and the maximum values).

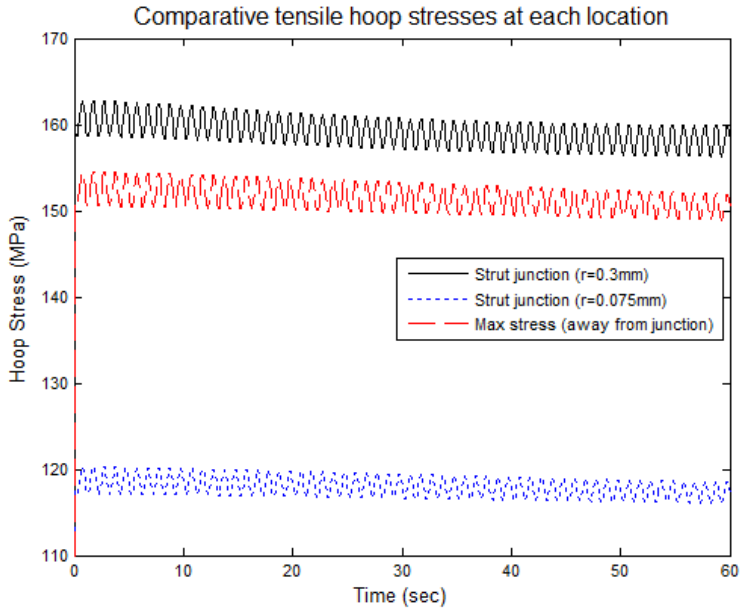

Figure 4.34: Hoop stresses due to tension at each of the three locations (i.e. each strut connection at the junctions and the maximum values).

The cyclic hoop strains at each location due to compression and tension are presented in Figures 4.35 and 4.36, respectively. As shown in Figure 4.35, the strains as a result of compression in the model are approximately the same at each strut connection, increasing from approximately 6% to 9% strain. Away from the strut connections, the strains increase from approximately 9% to 14%. Without a bar connecting the rings at the latter location, this reduces stability, thus an increase in strain along with stress as depicted previously, is observed. In tension, as shown in Figure 3.36, the strains that are observed at the strut connections do vary, however. On the opposite side the strut connection with the smaller radius, the strain increases from approximately 3.5% to 5% strain. At the opposite strut connection; the tensile strain increases from 5% to 7.5%. Away from the strut junction, the strain increases from 6.5%

to 9.5%. Also observed in Figure 4.36, it is apparent that degradation increases at each location, as the amplitude in each curve increases. This is supported by plotting the degradation over time in Figures 4.37 and 4.38, where Figure 4.37 represents degradation due to compressive strains at each location and the Figure 4.38 represents degradation due to tensile strains. As can be seen, the difference in degradation at each point (i.e. the order of least to greatest) corresponds to that observed in the strain response. Again, though a slow degrading model was utilized in this analysis, the greater curvature in the model causes the material to strain more rapidly and degrade in a fashion more similar to the fast degrading model observed in the cylindrical annulus.

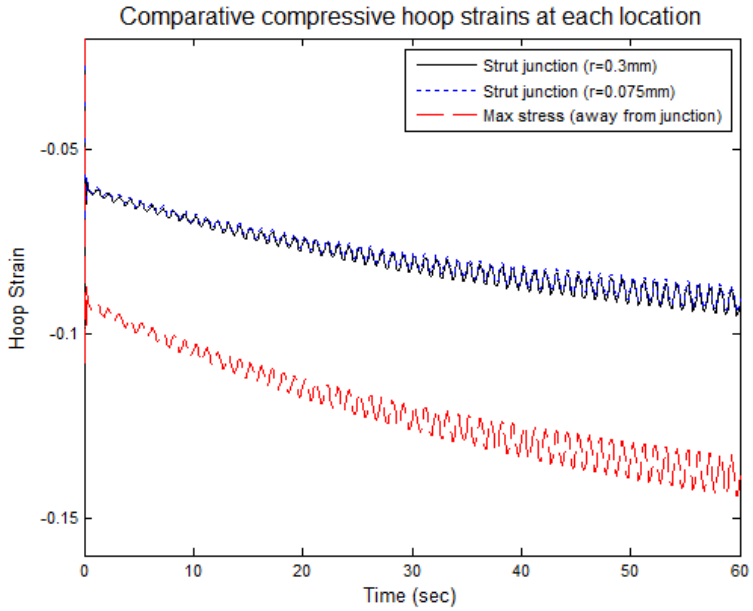

Figure 4.35 Hoop strains due to compression at each of the three locations (i.e. each strut connection at the junctions and the maximum values).

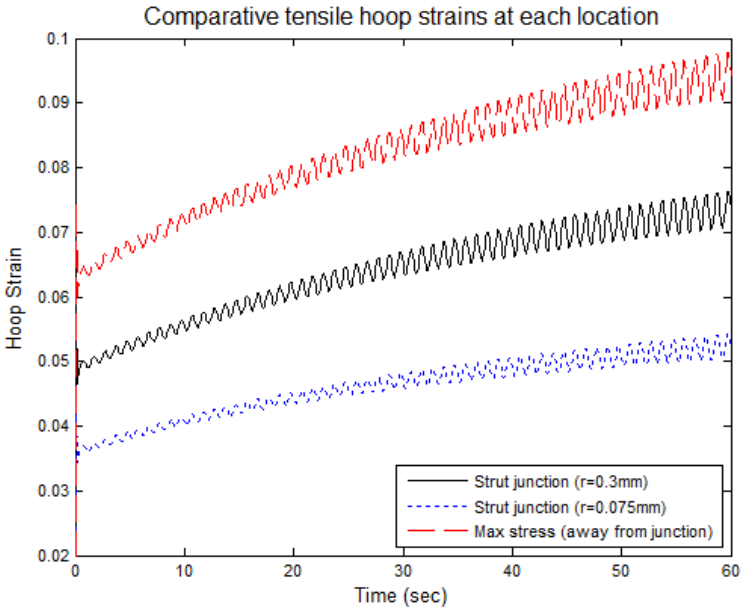

Figure 4.36 Hoop strains due to tension at each of the three locations (i.e. each strut connection at the junctions and the maximum values).

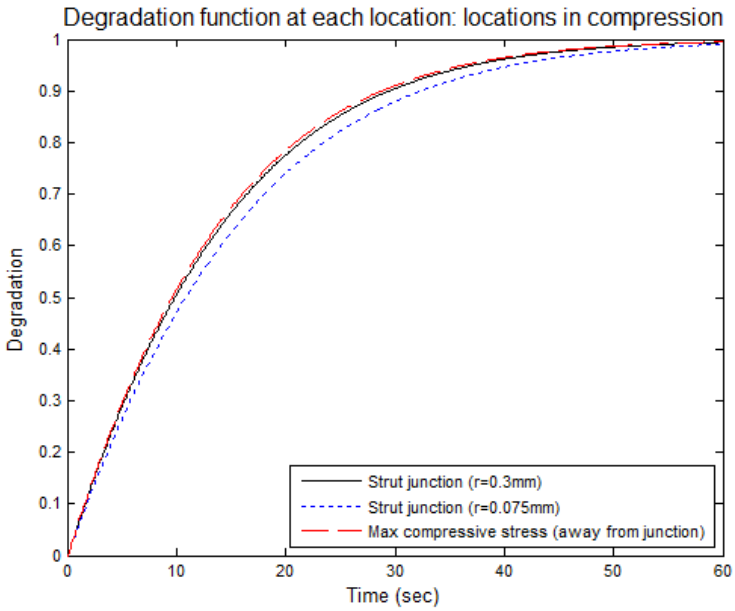

Figure 4.37: Degradation over time at each of the three locations due to compressive strains.

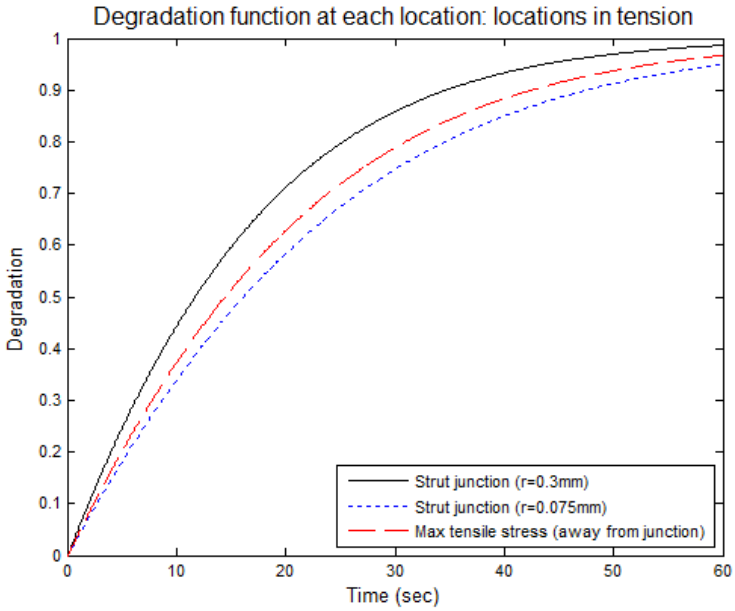

Figure 4.38: Degradation over time at each of the three locations due to tensile strains.

A comparison of each model analyzed in this study is presented in order to depict how the geometry affects the degradation. The degradation contours of each model are presented, illustrating the maximum and minimum values (1 and 0, respectively) of the scalar degradation variable and their respective locations. For each contour, the values of the degradation variable are presented at the time increment associated with a total time of 30 seconds. Figure 4.39 presents the contours of each model, depicting how the degradation occurs throughout the geometries of each. Figures 4.39a and 4.39b depict the contour for the cylindrical annulus. Two contours are plotted to for this model due to the vast difference in the degradation that occurs from the realistic models. Figure 4.39a depicts the contour where the range of the scalar degradation value is from 0 to 1. Because this model is subjected to far less strains than the realistic models, and thus far less degradation, very little degradation occurs at 30 seconds. Figure 4.39b depicts the

contour with a more refined range in the degradation. Here, the range is set from 0.045 to 0.0475 in order to show where the maximum degradation occurs and degradation is distributed throughout the model. The degradation away from the edges remains constant throughout the length of the model, with a maximum value much lower than that observed in the realistic stent models. Figures 4.39c and 4.39d depict the contours for the cross-hatched mesh model without inclusion of fillets and with fillets, respectively. As was previously shown, stress concentrations are at a maximum at the sharp edges in the model without fillets, with greater strains at this location. Hence, the strain-induced degradation values at the junctions in the cross-hatched mesh are greater in the model without fillets. It is also noted that due to the repeating patterns in the realistic stent geometries, only one section of the stent is needed to present the how the degradation varies throughout the model. Figure 4.39e presents the contour for the curvy geometry with repeating rings connected via struts. Due to the increased curvature in this model, this geometry exhibits the greatest amount of deformation at the curvatures without strut connections, thus the strain-induced degradation at these points are at a maximum.

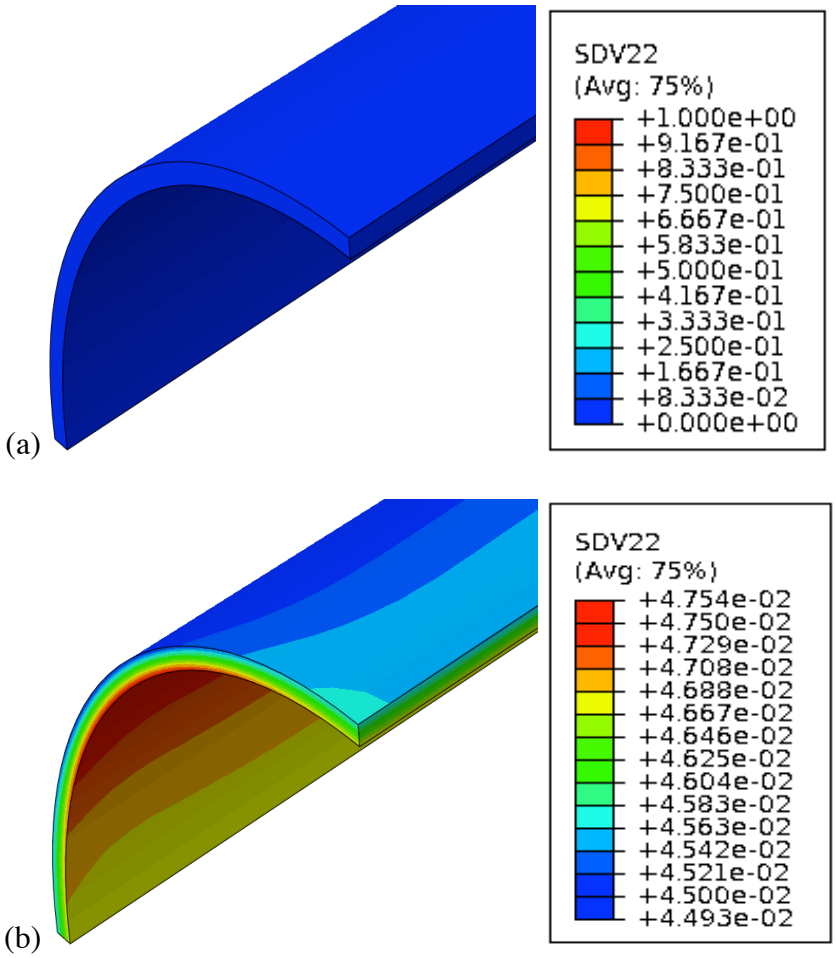

Figure 4.39: Degradation contours for the cylindrical annulus: (a) Contour with range of values from zero (no degradation) to 1 (maximum degradation) and (b) Contour with refined range of values (0.045 - 0.0475). Values taken at time t=30 seconds.

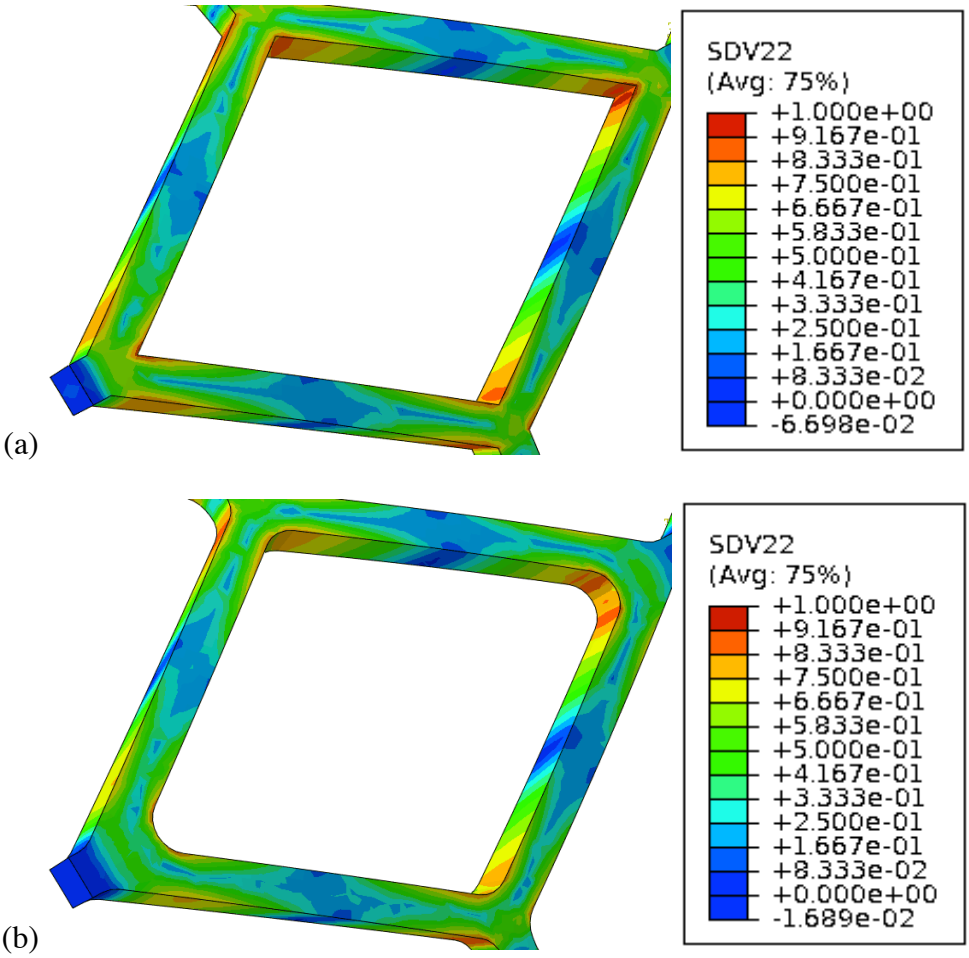

Figure 4.40: Degradation contours of the cross-hatched pattern stent geometry: (a) Model without inclusion of fillets and (b) Model with inclusion of fillets. Values taken at time t=30 seconds.

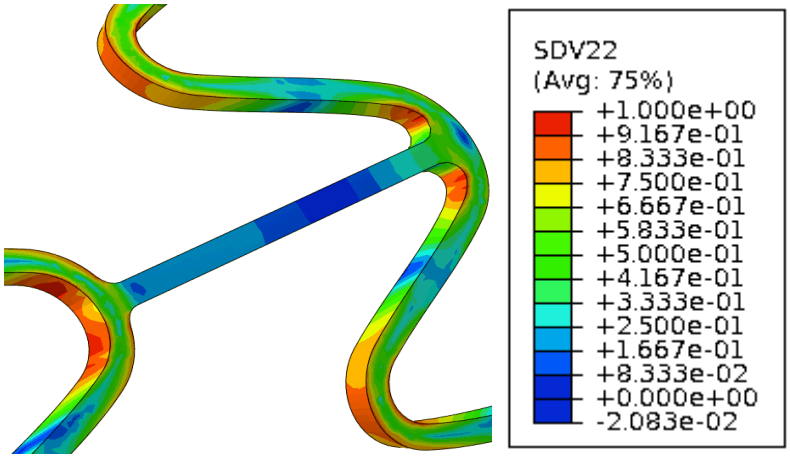

Figure 4.41: Degradation contour for the repeating curvy-ringed model. Values taken at time t=30 seconds.

CHAPTER V

SUMMARY OF RESULTS

5.1 Discussion of Studies

In the present studies, a cylindrical annulus with typical cardiac stent dimensions was analyzed under cyclic internal loading meant to mimic a healthy blood pressure, coupled with a constant external pressure to simulate the crushing effect of the arterial wall on a deployed stent. A comparison of two polymers with different time-dependent material properties was conducted, each at slow degradation and fast degradation. The degradation model utilized for the studies presented was a simplified model that is strain-induced, thus removing variables that are known to affect material properties of polymers over time, such as temperature and solution concentration. This simplification was done to focus on the development of a numerical algorithm to define the stress response of a homogeneous, isotropic, linear viscoelastic material and how the material deforms under cyclic loading conditions.

After conducting two different studies, ramped loading and creep-cyclic loading conditions, detailed results of how polymeric materials respond while undergoing degradation was able to be obtained. It was observed that the time-dependent properties of polyoxymethylene (POM) yield the material to have a higher stiffness than poly-L-lactic acid (PLLA) as it undergoes slower stress relaxation compared to PLLA, thus higher strains are observed in PLLA as predicted. As well, the repeated loading and unloading during cyclic analysis showed that POM dissipated more mechanical energy

that PLLA. In addition, the rate at which degradation occurs had a large effect on how the material deforms. While undergoing slow degradation, the strains oscillate over time with an amplitude that remained relatively constant. With fast degrading models, the amplitude in hoop strain showed to increase sharply, as expected. This was a result of the mechanical properties reducing toward 20% of their original value as defined in the degradation function.

Lastly, a study to examine how stress concentrations will develop in typical stent geometries was conducted. This analysis was conducted using two different geometries with dimensions consistent with metallic stents in use today, along with a slow degrading constitutive model and with PLLA material properties. The magnitude of stresses that occurred was much higher using typical stent geometries than with the simplified model. This was due to the curvatures that are introduced in the different models. For PLLA, this resulted in the hoop stresses after 1 minute of analysis exceeding the yield strength at the junctions in the model. The present study aims at understanding the viscoelastic and geometrical effects of the polymeric stents undergoing cyclic loading while the mechanical properties of the polymers degrade with time. It is clearly seen that the geometrical shapes of the tubular meshed stents induced non-uniform and localized stress/strains near the junctions, which could accelerate degradation at these locations. Ideally, the polymeric stents should degrade by surface erosion to maintain the integrity of stents during degradation and guarantee proper load transfer from the stents to the healing arterial walls. However, faster degradation at the junctions within the

tubular meshed stents could lead to early failure and breaking of the stents into pieces of polymers that flow through the bloodstream.

5.2 Further Research

As mentioned previously, the analyses of the degrading polymeric stents that were presented here were oversimplified. The idea of a biodegradable stent is to degrade until the healing artery can withstand the loading. This process is understood in literature of the subject matter to need to occur over a time period of roughly 6 months. Long-term material properties and degradation behaviors of the materials under various mechanical and non-mechanical stimuli are needed.

For further studies concerning the topic of biodegradable stents, inclusion of environmental factors that will affect degradation are recommended. These include temperature and effects due to moisture, since the material is deployed within the bloodstream of the human body. In addition, polymers deform in a nonlinear fashion under loading, thus the constitutive model for further studies should include nonlinearities that will certainly affect how the material degrades and deforms.

The geometrical model used for the majority of the study was simply a cylindrical annulus with typical diameter, length and thickness of stents currently on the market. This excluded failure modes in the analysis related to strut failure. To gain a better understanding of how the present constitutive model would affect real stent geometries, additional geometries that would reduce stress concentrations as observed in the last study should be analyzed. In addition, the two realistic geometries models were

designed using dimensions consistent with metallic stents. Because polymers are weaker materials, the thickness should be increased in the polymeric stent models. Furthermore, the effect of arterial wall pressure, which is time-dependent, should be incorporated to better understand the response and properly design the polymeric stents.

REFERENCES

[1] Agrawal, C., K. Haas, D. Leopold, and H. Clark. "Evaluation of Poly (L-lactic Acid) as a Material for Intravascular Polymeric Stents." *Biomaterials* 13.3 (1992): 176-82. Print.

[2] Bedoya, Julian, Clark A. Meyer, Lucas H. Timmins, Michael R. Moreno, and James E. Moore. "Effects of Stent Design Parameters on Normal Artery Wall Mechanics." *Journal of Biomechanical Engineering* 128.5 (2006): 757. Print.

[3] Duraiswamy, Nandini, Richard T. Schoephoerster, Michael R. Moreno, and JamesE. Moore. "Stented Artery Flow Patterns and Their Effects on the Artery Wall." *Annual Review of Fluid Mechanics* 39.1 (2007): 357-82. Print.

[4] Grabow, Niels, Carsten M. Bünger, Christine Schultze, Kathleen Schmohl, David P. Martin, Simon F. Williams, Katrin Sternberg, and Klaus-Peter Schmitz. "A Biodegradable Slotted Tube Stent Based on Poly(l-lactide) and Poly(4-hydroxybutyrate) for Rapid Balloon-Expansion." *Annals of Biomedical Engineering* 35.12 (2007): 2031-038. Print.

[5] Grabow, Niels, David P. Martin, Klaus-Peter Schmitz, and Katrin Sternberg. "Absorbable Polymer Stent Technologies for Vascular Regeneration." *Journal of Chemical Technology & Biotechnology* 85.6 (2010): 744-51. Web.

[6] "Heart Disease and Stroke Prevention." *Centers for Disease Control and Prevention*. Centers for Disease Control and Prevention, 21 July 2010. Web. 16 July 2014.

[7] Mollica, Francesco, Luigi Preziosi, and K. R. Rajagopal. *Modeling of Biological Materials*. Boston, MA: Birkhäuser, 2006. Print.

[8] Moore, James E., Joao S. Soares, and Kumbakonam R. Rajagopal. "Biodegradable Stents: Biomechanical Modeling Challenges and Opportunities." *Cardiovascular Engineering and Technology* 1.1 (2010): 52-65. Print.

[9] Moore, J.e., J. Bedoya, L.h. Timmins, C.a. Meyer, and M.r. Moreno. "Stented Artery Biomechanics and Device Design Optimization." *Journal of Biomechanics* 39 (2006): S402. Print.

[10] Muliana, Anastasia, and K.r. Rajagopal. "Modeling the Response of Nonlinear Viscoelastic Biodegradable Polymeric Stents." *International Journal of Solids and Structures* 49.7-8 (2012): 989-1000. Web.

[11] Mun, Sungho. "Numerical Computation of Convolution Integral for the Linear Viscoelasticity of Asphalt Concrete." *KSCE Journal of Civil Engineering* 10.3 (2006): 195-200. Print.

[12] Soares, João S., James E. Moore, and Kumbakonam R. Rajagopal. "Modeling of Deformation-Accelerated Breakdown of Polylactic Acid Biodegradable Stents." *Journal of Medical Devices* 4.4 (2010): 041007. Print.

[13] Soares, João S., Kumbakonam R. Rajagopal, and James E. Moore. "Deformation-induced Hydrolysis of a Degradable Polymeric Cylindrical Annulus." *Biomechanics and Modeling in Mechanobiology* 9.2 (2010): 177-86. Print.

[14] Soares, Joao F. "Constitutive Modeling for Biodegradable Polymers for Application in Endovascular Stents." Diss. Texas A&M U, 2008. Print.

[15] Timmins, Lucas H., Clark A. Meyer, Michael R. Moreno, and James E. Moore. "Effects of Stent Design and Atherosclerotic Plaque Composition on Arterial Wall Biomechanics." *Journal of Endovascular Therapy* 15.6 (2008): 643-54. Print.

[16] Tscharnuter, Daniel, and Anastasia Muliana. "Nonlinear Response of Viscoelastic Polyoxymethylene (POM) at elevated Temperatures." *Polymer* 54.3 (2013): 1208-217. Web.

[17] Venkatraman, Subbu S., Lay Poh Tan, Joe Ferry D Joso, Yin Chiang Freddy Boey, and Xintong Wang. "Biodegradable Stents with Elastic Memory." *Biomaterials* 27.8 (2006): 1573-578. Print.

[18] Venkatraman, Subbu, Tay L. Poh, Tjong Vinalia, Koon H. Mak, and Freddy Boey. "Collapse Pressures of Biodegradable Stents." *Biomaterials* 24 (2003): 2105-111. Web.

[19] Welch, Tre, Robert C. Eberhart, and Cheng-Jen Chuong. "Characterizing the Expansive Deformation of a Bioresorbable Polymer Fiber Stent." *Annals of Biomedical Engineering* 36.5 (2008): 742-51. Print.

[20] Wineman, A. S., and K. R. Rajagopal. *Mechanical Response of Polymers: An Introduction*. Cambridge: Cambridge UP, 2000. Print.

[21] Yun, Taeyoung. "Generalized Numerical Computation Method of the Convolution Integral for Rate-dependent Asphalt Concrete Mixtures." *KSCE Journal of Civil Engineering* 15.2 (2011): 257-60. Print.

APPENDIX A

UMAT FOR A DEGRADING LINEAR VISCOELASTIC MATERIAL

```
**********************************************************************
UMAT for an isotropic linear viscoelastic material undergoing degradation with N
number of Prony series. Mechanical properties are taken from literature. The Poisson's
ratio was determined assuming that the material is near incompressible.
**********************************************************************
C
      SUBROUTINE UMAT(STRESS,STATEV,DDSDDE,SSE,SPD,SCD,
     1 RPL,DDSDDT,DRPLDE,DRPLDT,
     2 STRAN,DSTRAN,TIME,DTIME,TEMP,DTEMP,PREDEF,DPRED,CMNAME,
     3 NDI,NSHR,NTENS,NSTATV,PROPS,NPROPS,COORDS,DROT,PNEWDT,
     4 CELENT,DFGRD0,DFGRD1,NOEL,NPT,LAYER,KSPT,KSTEP,KINC)
C
      INCLUDE 'ABA_PARAM.INC'
C
      CHARACTER*80 CMNAME
C
      DIMENSION STRESS(NTENS),STATEV(NSTATV),
     1 DDSDDE(NTENS,NTENS),DDSDDT(NTENS),DRPLDE(NTENS),
     2 STRAN(NTENS),DSTRAN(NTENS),TIME(2),PREDEF(1),DPRED(1),
```

```
     3 PROPS(NPROPS),COORDS(3),DROT(3,3),DFGRD0(3,3),DFGRD1(3,3)
      DIMENSION DSTRES(NTENS),D(3,3)
C
      DIMENSION En(10), taun(10), EG_n(10), ELAM_n(10)
      DIMENSION qij_n_t(6,10), qij_n_t1(6,10)
      DIMENSION qkk_n_t(10), qkk_n_t1(10)
      DIMENSION deij(6), deij_dt(6), deij_dt1(6)
      DIMENSION sum_qij(6)
C
      REAL A, alpha, eps_crit, mag_eps, d_t, d_t_his
      REAL term1, term2, exp
      REAL E_inf, EG_inf, ELAM_inf
      REAL sum_EGn, sum_ELAMn
C
C  Assign mechanical properties taken from literature.
C
      E0 = PROPS(1)
      ENU = PROPS(2)
      N = PROPS(3)
      DO K1 = 1,N
        En(K1) = PROPS(2*K1+2)
        taun(K1) = PROPS(2*K1+3)
```

```
      END DO
C
C  Initialize variables with zero value.
C
      DO K1 = 1,N
        EG_n(K1) = 0.
        ELAM_n(K1) = 0.
        qkk_n_t(K1) = 0.
        qkk_n_t1(K1) = 0.
        DO K2 = 1,NTENS
          qij_n_t(K2,K1) = 0.
          qij_n_t1(K2,K1) = 0.
        END DO
      END DO
      d_t_his = 0.
C
C  Read state variables from history.
C
      DO K1 = 1,N
        DO K2 = 1,NTENS
          ihis = ihis + 1
          qij_n_t(K2,K1) = STATEV(ihis)
```

```
      END DO
    END DO
C
    DO K1 = 1,N
      ihis = ihis + 1
      qkk_n_t(K1) = STATEV(ihis)
    END DO
C
    DO K1 = 1,NTENS
      ihis = ihis + 1
      deij_dt(K1) = STATEV(ihis)
    END DO
C
    ihis = ihis + 1
    dekk_dt = STATEV(ihis)
C
    ihis = ihis + 1
    d_t_his = STATEV(ihis)
C
C  Define the degradation function variables at time t.
C
    A = 0.5
```

```
      mag_eps = (STRAN(1)**2. + STRAN(2)**2. + STRAN(3)**2. +
     1  2.*STRAN(4)**2. + 2.*STRAN(5)**2. + 2.*STRAN(6)**2.)**.5
      eps_crit = 0.00247
C
C  Define when degradation occurs. At or below critical strain, no degradation. Above
C  critical strain, degradation occurs.
C
      IF (mag_eps.le.eps_crit) THEN
        d_t = d_t_his
      END IF
C
      IF (mag_eps.gt.eps_crit) THEN
        d_t = (DTIME*A*mag_eps + d_t_his)/(1. + DTIME*A*mag_eps)
      END IF
C
C  Define shear modulus and 2nd lame at n and as t goes to infinity.
C
      exp = 2.7182817459
      alpha = 0.8
      term1 = 1./(2*(1+ENU))
      term2 = 1./(3*(1-2*ENU)) - 1./(3*(1+ENU))
C
```

```
      sum_EGn = 0.
      sum_ELAMn = 0.
      DO K1 = 1,N
        EG_n(K1) = (En(K1)*(1. - alpha*d_t))*term1
        ELAM_n(K1) = (En(K1)*(1. - alpha*d_t))*term2
        sum_EGn = sum_EGn + EG_n(K1)
        sum_ELAMn = sum_ELAMn + ELAM_n(K1)
      END DO
C
      E_inf = E0
      EG_inf = (E_inf*(1. - alpha*d_t))*term1
      ELAM_inf = (E_inf*(1. - alpha*d_t))*term2
C
C  Define the incremental strains.
C
      DO K1 = 1,NTENS
        deij(K1) = DSTRAN(K1)
      END DO
      dekk = deij(1) + deij(2) + deij(3)
C
C  Sum the time-dependent portions (i.e. qij and qkk) of the constitutive model.
C
```

```
      DO K1 = 1,NTENS
        sum_qij(K1) = 0.
        DO K2 = 1,N
        sum_qij(K1) = sum_qij(K1) + qij_n_t(K1,K2)*
     1    (exp**(-DTIME/taun(K2)) - 1.) + EG_n(K2)*(DTIME/2.)*
     2    ((deij(K1)/DTIME)+ exp**(-DTIME/taun(K2))*deij_dt(K1))
        END DO
      END DO
C
      sum_qkk = 0.
      DO K2 = 1,N
        sum_qkk = sum_qkk + qkk_n_t(K2)*(exp**(-DTIME/taun(K2))
     1    - 1.) + ELAM_n(K2)*(DTIME/2.)*((dekk/DTIME) +
     2    exp**(-DTIME/taun(K2))*dekk_dt)
      END DO
C
C  Define the incremental stresses.
C
      DO K1 = 1,NDI
        DSTRES(K1) = 2.*EG_inf*deij(K1) + ELAM_inf*dekk +
     1    2.*sum_qij(K1) + sum_qkk
        STRESS(K1) = STRESS(K1) + DSTRES(K1)
```

```
      END DO
C
      DO K1 = NDI+1,NTENS
        DSTRES(K1) = 2.*EG_inf*deij(K1) + 2.*sum_qij(K1)
        STRESS(K1) = STRESS(K1) + DSTRES(K1)
      END DO
C
C  Calculate the consistent tangent modulus at time t.
C
      DO K1 = 1,NTENS
        DO K2 = 1,NTENS
          DDSDDE(K2,K1) = 0.
        END DO
      END DO
C
      DO K1 = 1,NDI
        DDSDDE(K1,K1) =2.*EG_inf + ELAM_inf + sum_EGn +
     1    0.5*sum_ELAMn
      END DO
C
      DO K1 = NDI+1,NTENS
        DDSDDE(K1,K1) = EG_inf + 0.5*sum_EGn
```

```
      END DO
C
      DO K1 = 1,NDI
        DO K2 = 1,NDI
          IF (K1.ne.K2) THEN
            DDSDDE(K1,K2) = ELAM_inf + 0.5*sum_ELAMn
          END IF
        END DO
      END DO
C
C  Calculate history variables at time t.
C
      DO K1 = 1,NTENS
        DO K2 = 1,N
          qij_n_t1(K1,K2)= qij_n_t(K1,K2)*exp**(-DTIME/taun(K2))
     1      + EG_n(K2)*(DTIME/2.)*((deij(K1)/DTIME) +
     2      exp**(-DTIME/taun(K2))*deij_dt(K1))
        END DO
      END DO
C
      DO K2 = 1,N
        qkk_n_t1(K2) = qkk_n_t(K2)*exp**(-DTIME/taun(K2)) +
```

```
     1    ELAM_n(K2)*(DTIME/2.)*((dekk/DTIME) +
     2    exp**(-DTIME/taun(K2))*dekk_dt)
      END DO
C
      DO K1 = 1,NTENS
        deij_dt1(K1) = deij(K1)/DTIME
      END DO
C
      dekk_dt1 = (deij(1) + deij(2) + deij(3))/DTIME
C
C  Store the updated state variables in statev arrays.
C
      ihis = 0
      DO K1 = 1,N
        DO K2 = 1,NTENS
          ihis = ihis + 1
          STATEV(ihis) = qij_n_t1(K2,K1)
        END DO
      END DO
C
      DO K1 = 1,N
        ihis = ihis + 1
```

```
      STATEV(ihis) = qkk_n_t1(K1)
    END DO
C
    DO K1 = 1,NTENS
      ihis = ihis + 1
      STATEV(ihis) = deij_dt1(K1)
    END DO
C
    ihis = ihis + 1
    STATEV(ihis) = dekk_dt1
C
    ihis = ihis + 1
    STATEV(ihis) = d_t
C
RETURN
    END
```

APPENDIX B

INPUT FILE FOR A CYCLICALLY LOADED CYLINDRICAL ANNULUS

```
*Heading
 Simulated loading of a linear viscoelastic stent model with degradation
** Job name: LVE_1_degr Model name: LVE_1_degr
*Part, name=Cylindrical_annulus
*End Part
*Instance, name=Cylindrical_annulus-1, part=Cylindrical_annulus
*Node
1,        -2.5,          0.,          10.
……
1312,          0.,    2.4000001,          0.
*Element, type=C3D8
1,  657,  658,  674,  673,    1,    2,   18,   17
……
600, 1295, 1296, 1312, 1311,  639,  640,  656,  655
*Nset, nset=Tube, generate
   1,  1312,     1
*Elset, elset=Tube, generate
  1,  600,    1
** Section: Solid_section
```

*Solid Section, elset=Tube, material=PLLA

,

*End Instance

*Nset, nset=yz_plane, instance=Cylindrical_annulus-1, generate

  16, 1312,   16

*Elset, elset=yz_plane, instance=Cylindrical_annulus-1, generate

  15, 600,   15

*Nset, nset=xz_plane, instance=Cylindrical_annulus-1, generate

   1, 1297,   16

*Elset, elset=xz_plane, instance=Cylindrical_annulus-1, generate

  1, 586,   15

*Nset, nset=xy_plane, instance=Cylindrical_annulus-1

 641, 642, 643, 644, 645, 646, 647, 648, 649, 650, 651, 652, 653, 654, 655,

656

 1297, 1298, 1299, 1300, 1301, 1302, 1303, 1304, 1305, 1306, 1307, 1308, 1309, 1310,

1311, 1312

*Elset, elset=xy_plane, instance=Cylindrical_annulus-1, generate

 586, 600,   1

*Elset, elset=_Outer_surf_S2, internal, instance=Cylindrical_annulus-1, generate

  1, 600,   1

*Surface, type=ELEMENT, name=Outer_surf

_Outer_surf_S2, S2

```
*Elset, elset=_Inner_surf1_S1, internal, instance=Cylindrical_annulus-1, generate
  1,  600,    1
*Surface, type=ELEMENT, name=Inner_surf1
_Inner_surf1_S1, S1
*Elset, elset=_Inner_surf2_S1, internal, instance=Cylindrical_annulus-1, generate
  1,  600,    1
*Surface, type=ELEMENT, name=Inner_surf2
_Inner_surf2_S1, S1
*Elset, elset=_Outer_S2, internal, instance=Cylindrical_annulus-1, generate
  1,  600,    1
*Surface, type=ELEMENT, name=Outer
_Outer_S2, S2
*End Assembly
*Amplitude, name=Amp_1, definition=PERIODIC
1,          6.283,          0.,          1.
          0.,          1.
**
** MATERIALS
*Material, name=PLLA
*Depvar
22,
*User Material, constants=7
```

1369.18, 0.45, 2., 353.18, 11.852, 277.64, 198.56

** BOUNDARY CONDITIONS

** Name: XY_symmetry Type: Displacement/Rotation

*Boundary

xy_plane, 3, 3

** Name: XZ_symmetry Type: Displacement/Rotation

*Boundary

xz_plane, 2, 2

** Name: YZ_symmetry Type: Displacement/Rotation

*Boundary

yz_plane, 1, 1

** --

** STEP: Apply Pressure

*Step, name="Apply Pressure", inc=100000

Application of external and internal pressures to the stent model

*Visco

0.1, 10000.,

*Solution Technique, type=QUASI-NEWTON

** LOADS

** Name: Arterial Pressure Type: Pressure

*Dsload

Outer, P, 0.20265

*Dsload

Inner1, P, 0.0133322

*Dsload, amplitude=BPS

Inner2, P, 0.00266644

** OUTPUT REQUESTS

**

**Restart, write, frequency=0

**

** FIELD OUTPUT: F-Output-1

**

*Output, field

*Element Output, directions=YES

E, S, SDV

**

*End Step